Pausing after clap reduces power required to fling wings apart at low Reynolds number

Vishwa T. Kasoju[1] **and Arvind Santhanakrishnan**[1,2]

[1] School of Mechanical and Aerospace Engineering, Oklahoma State University, Stillwater, OK 74078, United States of America

[2] Author to whom any correspondence should be addressed.

E-mail: `askrish@okstate.edu`

Abstract. The smallest flying insects such as thrips (body length $<$ 2 mm) are challenged with needing to move in air at chord-based Reynolds number (Re_c) on the order of 10. Pronounced viscous dissipation at such low Re_c requires considerable energetic expenditure for tiny insects to stay aloft. Thrips flap their densely bristled wings at large stroke amplitudes, bringing both wings in close proximity of each other at the end of upstroke ("clap") and moving their wings apart at the start of downstroke ("fling"). From high-speed videos of free take-off flight of thrips, we observed that their forewings remain clapped for approximately 10% of the wingbeat cycle before start of downstroke (fling stroke). We sought to examine if there are aerodynamic advantages associated with pausing wing motion after upstroke (clap stroke) and before downstroke (fling stroke) at Re_c=10. A dynamically scaled robotic clap and fling platform was used to measure lift and drag forces generated by physical models of solid (non-bristled) and bristled wings in single wing and wing pair configurations, for pause times ranging between 0% to 41% of the cycle. For solid and bristled wing pairs, pausing before the start of downstroke (fling stroke) dissipated vorticity generated at the end of upstroke (clap stroke). This resulted in decreasing the drag coefficient averaged across downstroke (fling stroke) and in turn reduced power requirements. Also, increasing the pause time resulted in a larger decrease of dimensionless power coefficient for the wing pair configurations as compared to the single wing configurations. Our findings show that wing-wing interaction observed in clap and fling motion of tiny insect wings is necessary to realize aerodynamic benefits of pausing before fling, via reducing the power required to clap and fling for a small compromise in lift.

Keywords: tiny insects, bristled wings, clap and fling, flapping flight, aerodynamics, thrips

Submitted to: *Bioinspir. Biomim.*

1. Introduction

Despite the roughly tenfold increase in wing length of a hawk moth compared to that of a fruit fly, the aerodynamic mechanisms underlying their free-flight are surprisingly similar. A vast number of studies examining flight aerodynamics of fruit flies and larger insects have identified the following mechanisms of lift generation: 1) delayed stall via the leading edge vortex (LEV) (Dickinson & Götz 1993, Ellington et al. 1996); 2) rotational lift (Dickinson et al. 1999, Sane & Dickinson 2002); 3) wing-wake interactions (Dickinson et al. 1999); and 4) wing-wing interaction during stroke reversal via clap-and-fling (Weis-Fogh 1973, Weis-Fogh 1975, Spedding & Maxworthy 1986). Far little is known about flight aerodynamics in entire families of miniature insects of body lengths ranging from 0.1 mm to 2 mm, such as thrips and several parasitoid wasps (e.g., *Trichogramma* spp. (Jalali et al. 2016) and fairyflies (Huber et al. 2008)). Miniature insects have been primarily examined by entomologists owing to their ecological and agricultural importance (Crespi et al. 1997, Terry 2001, Ullman et al. 2002, Whitfield et al. 2005, Jalali et al. 2016). From an engineering standpoint, studies of tiny insect flight can guide the development of biomimetic micro aerial vehicles (Liu et al. 2016).

Viscous dissipation of kinetic energy presents a significant constraint to the flight of tiny insects, where Reynolds number based on wing chord and tip velocity (Re_c) is on the order of 1 to 10 (Santhanakrishnan et al. 2014, Jones et al. 2016, Santhanakrishnan et al. 2018). At such low Re_c, these insects have to continually flap to stay aloft (Sane 2016). Multifold increase in drag coefficient has been reported for revolving (Santhanakrishnan et al. 2018) and translating (Miller & Peskin 2004) wings for $Re_c \leq 32$. At $Re_c \geq 120$ corresponding to flight of fruit flies and larger insects, a large LEV is formed at the start of a half-stroke and remains attached to the wing until the end of the half-stroke (Ellington et al. 1996, Birch et al. 2004). The trailing edge vortex (TEV) is detached from the wing and shed in the wake. The attached LEV delays stall and helps in lift generation (Dickinson et al. 1999, Ellington 1999). In contrast, both the LEV and TEV do not separate from a wing during linear translation (Miller & Peskin 2004) and revolution for $Re_c \leq 32$ (Santhanakrishnan et al. 2018). This LEV-TEV 'vortical symmetry' has been proposed to decrease lift in tiny insect flight (Miller & Peskin 2004), due to reduction in the time rate of change of the first moment of vorticity (Wu 1981).

Many previous studies (Miller & Peskin 2004, Sun & Yu 2006, Kolomenskiy et al. 2011) have investigated the effects of clap and fling mechanism using simplified motions and concluded that clap and fling augments lift force generation. Cheng & Sun (2019) computationally investigated biologically-observed wingbeat kinematics of tiny insects and found that drag was reduced by 6 to 10 times as that generated by idealized clap and fling kinematics, with no change in lift generation.

Despite the above aerodynamic challenges, several studies have reported controlled flight of thrips over short distances (Terry 2001, Whitfield et al. 2005, Morse & Hoddle 2006, Rodriguez-Saona et al. 2010, Riley et al. 2011). Examining biomechanical

adaptations used by tiny insects can help to understand how they are able to overcome fluid dynamic constraints. Two such key adaptations have been examined in several studies, including the presence of long bristles in their wings and obligatory use of wing-wing interaction in free-flight (clap-and-fling). Sunada et al. (2002) used dynamically scaled models undergoing translation and rotation and found little variations in forces between solid (non-bristled) and bristled wing designs. Force coefficients for the bristled wing model were found to be more compared to solid wing model, when using a reduced surface area to determine the coefficients of the bristled wing. Weihs & Barta (2008) and Davidi & Weihs (2012) found that a comb-like wing could comparatively generate forces similar to that of solid wings of same shape, while saving up to 90% of the wing weight. Recent studies (Lee & Kim 2017, Lee et al. 2018, Lee et al. 2020) have shown that a comb-like wing can provide aerodynamic benefit at small inter-bristle gaps, owing to the formation of diffused shear layers around the bristles that block flow from leaking through the gaps. However, most of these studies used a single bristled wing model and did not address wing-wing interaction used in free-flight of tiny insects (Lehmann et al. 2005).

Santhanakrishnan et al. (2014) performed 2D computational simulations of clap-and-fling at Re_c corresponding to tiny insect flight. By approximating bristled wings as porous surfaces, this study found that bristled wings can provide substantial drag reduction when compared to solid wings during clap-and-fling. Jones et al. (2016) modeled wing bristles as 2D cylinder arrays and showed that bristled reduce the force required to fling the wings apart during wing-wing interaction. In our recent study (Kasoju et al. 2018), we experimentally examined the inter-bristle flow during clap-and-fling for bristled wing models with varying inter-bristle gap. When compared to a solid wing model, we found that bristled wings provide aerodynamic benefit through larger drag reduction and disproportionally lower lift reduction. Ford et al. (2019) found that thrips wings show a preference for smaller membrane area compared to the total wing area, and that wings with smaller membrane areas provide larger aerodynamic benefit during clap-and-fling at Re_c corresponding to tiny insect flight. Collectively, these studies show that combining biomechanical adaptations in wing kinematics (clap-and-fling) and wing morphology (bristles) can provide aerodynamic benefit to flapping flight at the scale of the smallest insects.

In addition to the obligatory use of clap-and-fling, tiny insects have been observed to use a shorter upstroke duration and a longer downstroke duration (Santhanakrishnan et al. 2014). Such an asymmetric reduction of upstroke duration can lower the time where loss of lift occurs, as most of the lift in flapping flight of insects is generated during the downstroke (Sane 2003). Ellington (1975) observed that the tiny chalcid wasp *Encarsia formosa* paused wing motion at the end of upstroke (clap) for about 10% of total cycle time (taken here as the sum of upstroke and downstroke time). He proposed that pausing at the end of upstroke (clap stroke) could potentially promote shedding and advection of vortices away from the wing before the start of fling, and reduce the mechanical energy required for fling. These hypotheses were not tested in his study, and

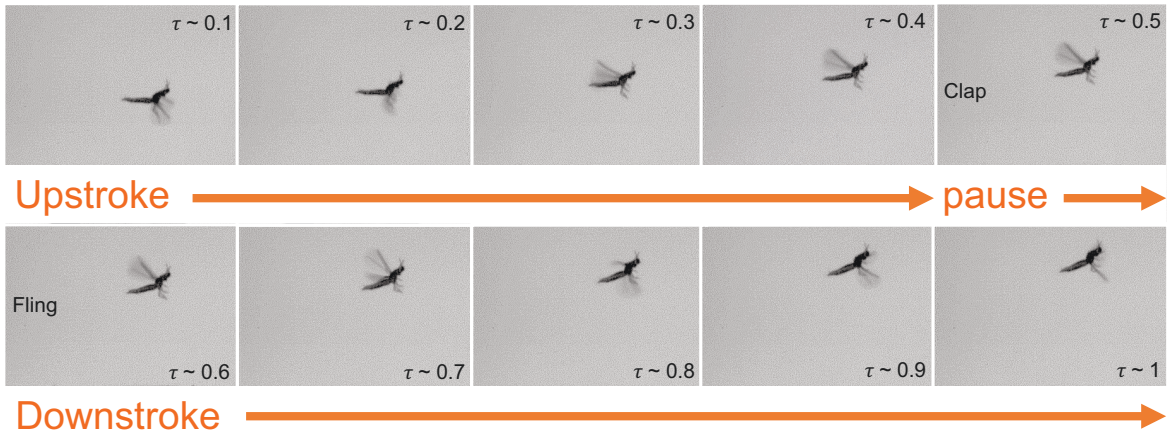

Figure 1. Successive snapshots of thrips in free take-off flight during one cycle (τ denotes fraction of cycle time). At the end of upstroke (τ = 0.4-0.5), both fore wings were brought in close proximity of each other ('clap'). The wings paused for approximately 10% of flapping cycle before the start of downstroke ('fling'). See Table 1 for more information.

the aerodynamic implications of pausing after upstroke (clap stroke) are unknown. In this study, we experimentally examine force generation during clap-and-fling at Re_c=10 across varying pause duration following the upstroke (clap stroke) phase. Our tests were conducted using a dynamically scaled robotic model outfitted with bristled wing and solid wing physical models (Kasoju et al. 2018, Ford et al. 2019). 2D particle image velocimetry (PIV) measurements were used to examine the evolution and dissipation of flow structures around the wings during the pause following the upstroke (clap stroke) phase.

2. Materials and methods

2.1. Free-flight recordings of thrips

Thrips were collected in Chapel Hill, NC, USA, during early June, 2017 from daylilies, gardenia and Azaleas flowers. The flowers with insects were then brought to recording arena and filmed within few hours of their collection. We used a procedure similar to that described in the study by Santhanakrishnan et al. (2014) for filming free take-off flight. A pipette tip was placed on top of an insect to allow it to crawl inside the tube. A single high-speed camera (Phantom v7.1, Vision Research, Wayne, NJ, USA) was used for filming. The camera was fitted with a 55 mm micro-Nikkor lens, a Nikon PB-5 bellows with variable extension, and a 27.5 mm extension tube. The pipette tip with thrips was placed upside-down in the camera field of view, and we waited for the thrips to crawl out of the tube and take-off from the tip. The field of view was illuminated using a red light emitting diode (LED) array. A white diffuser placed in front of the camera aperture, with the pipette tip located in between camera and the LED array. Free take-off flight of thrips were filmed at different frame rates with a shutter duration

ranging between 15–30 μs (Table 1).

Five high-speed video recordings (representative snapshots shown in Figure 1) were digitized and analysed in ImageJ (National Institutes of Health, Bethesda, MD, USA) for calculating the pause time between the end of upstroke (clap) and start of downstroke (fling), and the results are provided in Table 1. The five raw videos that were used for analysis are provided as supplementary material (Movies S1-S5). The average pause time from the five recordings was calculated to be 11±2% of the total cycle time. This calculated pause time was close to that of *E. formosa* (10% of cycle time) reported by Ellington (1975).

Table 1. Pause duration analyzed between end of upstroke and start of downstroke for several high speed video recordings.

Trial	Recording rate [fps]	Cycle time [ms]	Pause time [% cycle]
1	3000	4.67	14.3
2	4000	5.25	9.5
3	4000	5.5	9.1
4	4000	4.75	10.5
5	4700	4.04	10.5

2.2. Test facility

The dynamically scaled robotic wing platform used in this study has been used before (Kasoju et al. 2018, Ford et al. 2019) and is described briefly here. The robotic platform consists of four 2-phase hybrid stepper motors with integrated encoders (ST234E, National Instruments Corporation, Austin, TX, USA) mounted on an acrylic tank with 0.51 m x 0.51 m cross-section, and 0.41 m in height. These motors were used to prescribe the motion of 2 physical wing models. The four stepper motors were controlled by a multi-axis controller (PCI-7350, National Instruments Corporation, Austin, TX, USA) via custom programs written in LabVIEW software (National Instruments Corporation, Austin, TX, USA). Two stepper motors were dedicated to each wing to perform rotation and translational motion with help of bevel gear pairs and rack and pinion mechanism, respectively.

2.3. Physical models

A bristled wing of membrane width 7 mm, with symmetric bristle lengths on either side of a membrane (Figure 2A) was laser cut from an optically clear acrylic sheet of thickness 3.18 mm. The bristles were cut to required length from 304 stainless steel wires of uniform diameter (D) of 0.31 mm and were glued on top of the acrylic membrane with inter-bristle spacing (G) to bristle diameter (D) ratio (i.e., G/D) of 5 (Figure 2A). The commonly observed range of G/D in tiny insects is 4-12 (Jones et al. 2016). In order to

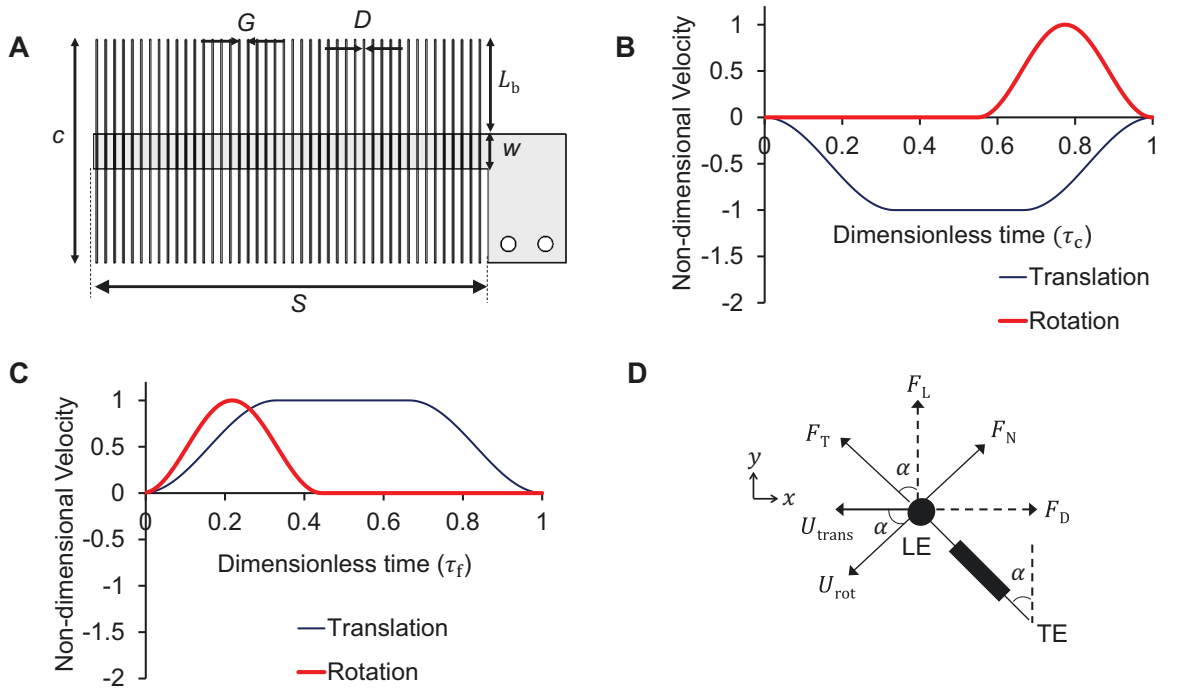

Figure 2. (A) Bristled wing model of chord length (c)=45 mm, wing span (S)=81 mm, inter-bristle spacing (G)=1.83 mm, bristle diameter(D)=0.31 mm, length of bristle (L_b)=19 mm and membrane width (w)=7 mm. A solid wing model (without bristles) with the same chord (c) and span (S) lengths as that of the bristled wing was also tested. (B) and (C) show the time-varying motion profile prescribed for motion of a single wing during upstroke (clap stroke) and fling, respectively, based on a previous study by Miller and Peskin (2005). The thin line indicates the wing translational motion while the thick line represents the wing rotation. (D) The sectional view of a bristled wing model (referred here as "chordwise view") with directions of measured tangential (F_T) and normal forces (F_N) experienced during rotation by angle α. Lift (F_L) and drag (F_D) forces were measured by taking components of F_T and F_N in the vertical and horizontal directions, respectively. τ_c=dimensionless upstroke (clap stroke) time; τ_f=dimensionless downstroke (fling stroke) time; LE=leading edge; TE=trailing edge; U_{trans}=translational velocity at wing tip; U_{rot}=rotational velocity at wing tip; x,y are global horizontal and vertical coordinate axes.

fit a biologically relevant number of bristles (n=88) within a fixed span (S) of 81 mm, while also ensuring that Reynolds number based on bristle diameter (Re_b) was in the biologically relevant range of 0.01 to 0.07, we chose bristle diameter (D) of 0.31 mm. For a rectangular bristled wing with symmetric bristle lengths on either side of a solid membrane, G, D, S can be related to the total number of bristles (n, including both sides of a solid membrane) via the relation:

$$\frac{G}{D} = \left(\frac{2S}{nD}\right) - 1 \tag{1}$$

We obtained G/D=5 using the above relation, which is in the biologically relevant range. Also, an equivalent solid wing pair with the same chord and span lengths as the bristled

wing model was laser cut from a 3.18 mm thick acrylic sheet. Each wing of the wing pair being tested was attached to custom made aluminum L-brackets and completely immersed inside the acrylic tank (described above under test facility) using 6.35 mm diameter stainless steel D-shafts.

Among our physical models, we have not observed the solid wing and the solid membrane of the bristled wing to deform. The solid wings and the membrane of the bristled wings as the wings were fabricated from acrylic sheets. The bristles used in our physical bristled wing models were cut from 304 stainless steel wires, which are thin and have the possibility of bending. However, while performing flow visualization using PIV, we did not observe the bristles to bend during wing motion. This could be due to the high viscosity of the fluid medium (glycerin) not allowing the steel wires to noticeably bend.

2.4. Wing kinematics

A modified version of 2D clap and fling kinematics that was initially developed by Miller & Peskin (2005) was prescribed for wing motion in the robotic model (Figure 2B,C). The motivation behind using this kinematics is that it provides a simplified representation of the complex three-dimensional wing kinematics of an insect, with particular emphasis on the portion of the wing motion from the end of the upstroke and the start of the downstroke, i.e., the duration of upstroke (clap stroke) and downstroke (fling stroke) motion. However, these kinematics do not account for 3D flapping revolution of a real insect during the upstroke and downstroke. The rotational velocity profile should be considered as a simplification, and recent studies (Lyu et al. 2019, Cheng & Sun 2018, Cheng & Sun 2021) have shown that tiny insects do not employ symmetrical acceleration/deceleration during their wing motion. Similar forms of these kinematics have been used in many previous studies (Santhanakrishnan et al. 2014, Arora et al. 2014, Jones et al. 2016, Kasoju et al. 2018, Ford et al. 2019). The wings were made to rotate and translate simultaneously with 100% overlap prescribed between rotation and translation during both upstroke (clap stroke) and downstroke (fling stroke) phases. Wing rotation during upstroke (clap stroke) was adjusted such that rotation ended exactly when the wings stopped translating, as shown in Figure 2B. During fling, wings were made to start rotation and translation at the same time, as shown in Figure 2C. Arora et al. (2014) previously examined the effects of varying the percentage of overlap between rotation and translation on forces generation, and reported increase in force coefficients with increasing overlap during upstroke (clap stroke) and downstroke (fling stroke). This was the rationale for choosing maximum possible overlap for both upstroke (clap stroke) and downstroke (fling stroke) in this study. Figure 2B,C show prescribed non-dimensional velocities as a function of dimensionless time (τ_c,τ_f) during upstroke (clap stroke) and downstroke (fling stroke), respectively. The dimensionless times for each phase (upstroke (clap stroke) or downstroke (fling stroke)) are indicated as the ratio of instantaneous time to total time of a specific phase (upstroke (clap stroke)

or downstroke (fling stroke)). Note that the kinematics presented here are for a single wing performing upstroke (clap stroke) and downstroke (fling stroke). The kinematics for the other wing were identical but in opposite directions. The inter-wing spacing between the wings was set to 10% of chord, which is similar to those observed in free flight recordings of thrips (Santhanakrishnan et al. 2014). While the terms 'clap' and 'fling' are traditionally referred to in the context of wing pairs, we use these terms also for a single wing that is prescribed to move using the same kinematics as that of a wing pair. Comparison of a one-winged upstroke (clap stroke) and downstroke (fling stroke) motion against a two-winged (i.e., traditional) clap and fling motion has been performed previously for solid wings (Miller & Peskin 2005), and we employ a similar comparative assessment in this study.

2.5. Test conditions

Force measurements and flow visualization were conducted on a single wing (solid and bristled) and a wing pair (solid and bristled) for 5 pause times (0%, 9%, 17%, 23%, 41% of the entire cycle time). We included 9% pause time so as to mimic the pause duration observed from high-speed video recordings of the free take-off flight of thrips (Figure 1, Table 1). The total cycle time is calculated as sum of upstroke (clap stroke) time, pause time and downstroke (fling stroke) time, in units of milliseconds (ms). Re_c=10 was maintained as a constant across all test conditions, where Re_c was based on steady translational velocity (U_{ST}) of the wing and chord length (c). The acrylic tank described in test facility above was filled with 99% glycerin solution to obtain Re_c=10. The kinematic viscosity (ν) of the 99% glycerin solution used in this study was measured using a Cannon-Feske routine viscometer (size 400, Cannon Instrument Company, State College, PA, USA) to be 706×10^{-6} m^2/s. The density of the 99% glycerin solution was measured to be 1260 kg/m^3. The Reynolds number based on bristle diameter (Re_{b}) was calculated to be 0.067 using the relation:

$$Re_{\mathrm{b}} = \frac{U_{\mathrm{ST}} D}{\nu} \tag{2}$$

and is within the biologically relevant range of 0.01-0.07 for tiny insect flight (Jones et al. 2016).

2.6. Force measurements

Forces on the wings were measured using uniaxial strain gauges bonded to the L-brackets (wing mount). The custom L-brackets were designed to measure forces in perpendicular (i.e., normal) and parallel (i.e., tangential) directions to the wing. The tangential force (F_{T}) and normal force (F_{N}) were then resolved along the global horizontal axis (x-axis) to obtain drag force (F_{D}) and vertical axis (y-axis) to obtain lift force (F_{L}) (Figure 2D). Separate L-brackets were used for measuring lift and drag as described in a previous study (Kasoju et al. 2018). A data acquisition board (NI USB-6210, National Instruments Corporation, Austin, TX, USA) was used to acquire the strain gauge

voltage data and angular position of the wings at a sample rate of 10 kHz throughout the entire cycle (includes upstroke (clap stroke) time, pause time and downstroke (fling stroke) time). We used the same processing procedures as used in Kasoju et al. (2018) and Ford et al. (2019). The raw data was filtered in MATLAB (The Mathworks Inc., Natick, MA, USA) using a third order low-pass Butterworth filter with a cutoff frequency of 24 Hz. The lift and drag brackets were calibrated manually and the calibrations were applied to the filtered voltage data. The forces were then resolved along global horizontal (drag force) and vertical (lift force) directions. We note that forces were only recorded on a single wing of a wing pair, with the assumption that force generation by other wing was symmetrical and equal in magnitude because the motion was symmetrical.

Dimensionless lift (C_{L}) and drag (C_{D}) coefficients were calculated as:

$$C_{\mathrm{L}} = \frac{F_{\mathrm{L}}}{\frac{1}{2}\rho U_{\mathrm{ST}}^2 A} = \frac{F_{\mathrm{T}}\cos\alpha + F_{\mathrm{N}}\sin\alpha}{0.5\rho U_{\mathrm{ST}}^2 A} \tag{3}$$

$$C_{\mathrm{D}} = \frac{F_{\mathrm{D}}}{\frac{1}{2}\rho U_{\mathrm{ST}}^2 A} = \frac{F_{\mathrm{T}}\sin\alpha + F_{\mathrm{N}}\cos\alpha}{0.5\rho U_{\mathrm{ST}}^2 A} \tag{4}$$

where F_{L} and F_{D} are the lift and drag forces measured along horizontal (in the direction perpendicular to wing motion) and vertical directions, respectively (in Newtons), U_{ST} represents steady translational velocity, ρ is density of the fluid medium and A represents the effective wing surface area (4.05×10^{-3} m^2) for both the solid and bristled wing. The reason for using effective surface area for the bristled wing, as opposed to a reduced surface area (excluding gaps between the bristles), is because a reduced surface area implicitly assumes that flow through the bristles is mostly identical to the ideal/inviscid case without allowing the possibility that flow can incompletely leak through the gaps between the bristles on account of viscous interactions (Kasoju et al. 2018). Standard deviations were calculated across 30 consecutive cycles for C_{L} and C_{D}, and the force coefficients were averaged across all cycles. In addition, phase-averaged force coefficients ($\overline{C_{\mathrm{L,clap}}}$, $\overline{C_{\mathrm{L,fling}}}$, $\overline{C_{\mathrm{D,clap}}}$, $\overline{C_{\mathrm{D,fling}}}$) were calculated in upstroke (clap stroke) and downstroke (fling stroke) phases separately. It is important to note that the term "phase-average" in calculation of $\overline{C_{\mathrm{L,clap}}}$, $\overline{C_{\mathrm{D,clap}}}$, $\overline{C_{\mathrm{L,fling}}}$, $\overline{C_{\mathrm{D,fling}}}$ is referenced in terms of upstroke (clap stroke) and downstroke (fling stroke) phases, so that the averaging was performed in time over the duration of upstroke (clap stroke, τ_{c} in Figure 2B) or downstroke (fling stroke, τ_{f} in Figure 2C). Cycle-averaged force coefficients ($\overline{C_{\mathrm{L,net}}}$, $\overline{C_{\mathrm{D,net}}}$) were calculated by averaging across the time period of the entire cycle, including clap, pause and fling phases. Standard deviations and averages for phase-averaged and cycle-averaged coefficients were calculated across all 30 cycles. Since the direction of drag force acting on the wings were in opposite direction for upstroke (clap stroke) and downstroke (fling stroke) phases, we used absolute values of the sum of C_{D} during upstroke (clap stroke) phase, pause time and downstroke (fling stroke) phase separately. The cycle-averaged net drag coefficient was calculated using trapezoidal rule in MATLAB and is presented here in an integral form as:

$$\overline{C_{\mathrm{D,net}}} = \int_0^1 C_{\mathrm{D}}(\tau)\, d\tau \tag{5}$$

and we calculated cycle-averaged net lift coefficient as:

$$\overline{C_{\mathrm{L,net}}} = \int_0^1 C_{\mathrm{L}}(\tau)\, d\tau \tag{6}$$

Similar to force coefficients, the power coefficient (C_{P}) was calculated using the equation:

$$C_{\mathrm{P}} = \frac{\text{Power}}{\frac{1}{2}\rho U_{\mathrm{ST}}^2 A} = \frac{F_{\mathrm{D}}\, U_{\mathrm{total}}}{\frac{1}{2}\rho U_{\mathrm{ST}}^3 A} \tag{7}$$

where $U_{\mathrm{total}} = U_{\mathrm{trans}} + U_{\mathrm{rot}} \cos\alpha$. U_{trans} and U_{rot} represents the wing tip velocity during translation and rotation, respectively, and α represents the wing rotation angle shown in Figure 2D. Similar to $\overline{C_{\mathrm{L,net}}}$ and $\overline{C_{\mathrm{D,net}}}$, cycle-averaged net power coefficient ($\overline{C_{\mathrm{P,net}}}$) was calculated by averaging across the time period of the entire cycle (including the clap, pause and fling phases) using the equation:

$$\overline{C_{\mathrm{P,net}}} = \int_0^1 C_{\mathrm{P}}(\tau)\, d\tau \tag{8}$$

2.7. Flow visualization

2D time-resolved PIV (2D TR-PIV) were conducted to visualize and measure the flow generated during the upstroke (clap stroke) phase, pause duration and downstroke (fling stroke) phase by the solid and bristled wings (single wing and wing pairs) along chordwise direction at the mid-span location (wings in chordwise view similar to Figure 2D). 2D TR-PIV measurements were acquired for both wing models (solid and bristled) at all test conditions (0%, 9%, 17%, 23%, 41% pause time). A single cavity Nd:YLF laser (Photonics Industries International, Inc., Bohemia, NY, USA) was used for illumination that provided a 0.5 mm diameter beam of 527 nm in wavelength. A thin laser sheet (thickness ≈ 3-5 mm) was generated from the beam using a cylindrical lens of 10 mm focal length. A high-speed complementary metal-oxide-semiconductor (CMOS) camera with a spatial resolution of 1280x800 pixels, maximum frame rate of 1630 frames/s, and pixel size of 20x20 microns (Phantom Miro 110, Vision Research Inc., Wayne, NJ, USA) was used for acquiring raw TR-PIV images. This camera was fitted with a 60 mm constant focal length lens (Nikon Micro Nikkor, Nikon Corporation, Tokyo, Japan). Hollow glass spheres of 10-micron diameter (110P8, LaVision GmbH, Göttingen, Germany) were used as seeding particles (Kasoju et al. 2018, Ford et al. 2019). 100 evenly spaced images were acquired at a recording rate of 90 Hz during the upstroke (clap stroke) and during the downstroke (fling stroke). The raw images were processed using DaVis 8.3.0 software (LaVision GmbH, Göttingen, Germany) using the following cross-correlation settings: one pass with an interrogation window of size 64x64 pixels and two subsequent passes with interrogation window of size 32x32 pixels, each with 50% overlap. The processed 2D TR-PIV images were phase-averaged over 5 non-consecutive cycles. We note the distinction in the "phase-average" term used in the context of 2D TR-PIV measurements against those used in the context of force measurements (described previously). With respect to

2D TR-PIV measurements, averaging was performed across 5 non-consecutive cycles at a fixed time instant (unlike "phase-averaging" of force measurements across the time period of the upstroke (clap stroke) or downstroke (fling stroke) phase, as in $\overline{C_{\mathrm{L,clap}}}$, $\overline{C_{\mathrm{D,clap}}}$, $\overline{C_{\mathrm{L,fling}}}$, $\overline{C_{\mathrm{D,fling}}}$). Following phase-averaging, 2D velocity vector fields were exported for calculating circulation (Γ) of the LEV and the TEV on a single wing of the imaged wing pair. Γ was calculated for all time points acquired during upstroke (clap stroke) and downstroke (fling stroke) separately using an in-house MATLAB script using Stokes' equation:

$$\Gamma = \int\int \omega_z dxdy \tag{9}$$

where ω_z represents the out-of-plane (z-component) of vorticity at the leading or trailing edges calculated from exported velocity vector fields and $dxdy$ represents the vorticity region for either the LEV or the TEV. For a particular pause condition, the maximum absolute values of ω_z (i.e., $|\omega_z|$) at both LEV and TEV of a bristled wing were identified. Similar to Ford et al. (2019) and Kasoju & Santhanakrishnan (2021), a $10\%|\omega_z|$ high-pass cut-off was next applied to isolate the vortex cores on a solid or a bristled wing model (single wing or wing pair) for that pause condition. Γ of LEV or TEV was then calculated by selecting a region of interest (ROI) by drawing a box around a vortex core. A custom MATLAB script was used to automate the process of determining the ROI (Samaee et al. 2020). Essentially, we started with a small square box of 2 mm side and compared the Γ value with that of a bigger square box of 5 mm side. If the circulation values matched between the 2 boxes, then we stopped further iteration. If the circulation values did not match between the 2 boxes, we increased the size of the smaller box by 3 mm and iterated the process. When calculating Γ of a specific vortex (LEV or TEV), we ensured that ω_z of the oppositely-signed vortex was zeroed out. For example, ω_z of the negatively-signed TEV was zeroed out when calculating the Γ of the positively-signed LEV on the right wing of a wing pair in downstroke (fling stroke). This allowed us to work with one particular vortex at a time and avoids contamination of the Γ estimation, if the box were to overlap with the region of the oppositely-signed vortex. Γ was determined for the right-hand side wing only, with the assumption that circulation for the left wing will be equivalent in magnitude but oppositely signed. Note that the left wing motion is symmetric to right wing making our assumption justifiable.

2D phase-locked PIV (2D PL-PIV) measurements were acquired for wing models along a spanwise plane (similar to 2D PL-PIV in Kasoju et al. (2018)) located at 50% of bristle length (L_{b}), measured from the membrane to the leading edge of the wing (Figure 2A). A double-pulsed, single-cavity Nd:YAG laser (Gemini 200-15, New Wave Research, Fremont, CA) with wavelength of 532 nm, maximum repetition rate of 15 Hz, and pulse width in the range of 3–5 ns was used for illumination in the PL-PIV measurements. A 10 mm focal length cylindrical lens was used to generate a thin laser sheet (thickness $\approx$ 3-5 mm). Raw PL-PIV images were acquired using a scientific CMOS (sCMOS) camera, with a maximum spatial resolution of 2600x2200 pixels at a frame rate of 50 frames/s, and a maximum pixel size of 6.5x6.5 microns (LaVision Inc.,

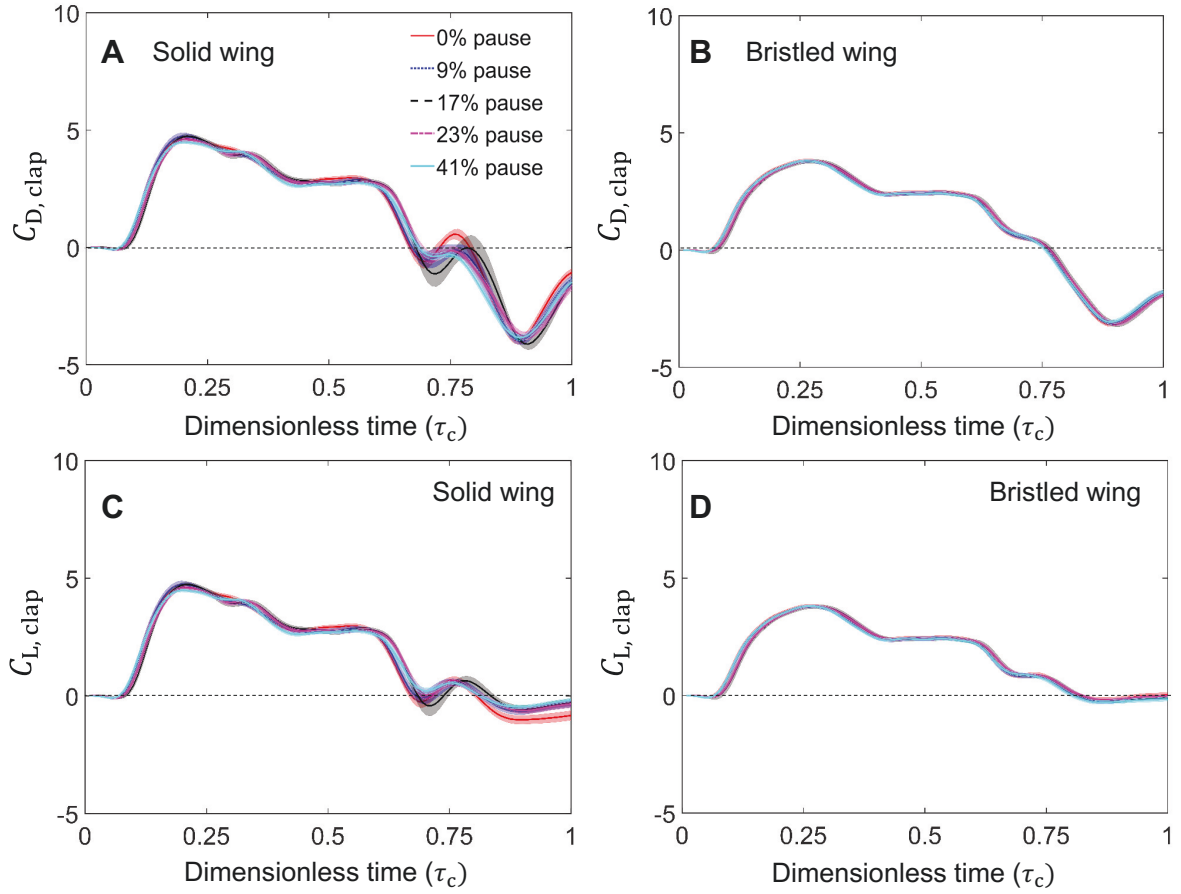

Figure 3. Force coefficients during upstroke (clap stroke) for a single wing at Re_c=10 with shading around each curve representing range of ±1 standard deviation for that particular data (across 30 cycles). (A) and (C) show the drag coefficient (C_D) and lift coefficient (C_L), respectively, during upstroke (clap stroke) (τ_c) for the solid wing model at various pause times. (B) and (D) show the drag coefficient (C_D)and lift coefficient (C_L) respectively during upstroke (clap stroke) (τ_c) for the bristled wing model at various pause times.

Ypsilanti, MI, USA). The 60 mm lens used in TR-PIV measurements was also used for PL-PIV measurements, and the camera was focused on seeding particles (hollow glass spheres, 10-micron diameter) along the laser plane (Kasoju et al. 2018). Raw image pairs were acquired at 7 time points in downstroke (fling stroke) at equally spaced time steps of 12.5% of stroke times (τ_f). The laser pulse separation between the images of an image pair were estimated based on 6-8 pixels of particle movement from one image to other image. For each wing model tested at Re_c=10, 5 image pairs were acquired at each time point in downstroke (fling stroke) cycle from 5 cycles of upstroke (clap stroke) and downstroke (fling stroke). These raw image pairs were processed using DaVis 8.3.0 software (LaVision GmbH, Göttingen, Germany) and then averaged for each time point. The post-processing parameters for 2D PL-PIV measurements were the same as those described earlier in 2D TR-PIV. The averaged processed images were exported to quantify the amount of fluid leaked through the bristles along the wing

span. (Cheer & Koehl 1987) estimated the amount of fluid leaking through a pair of cylinders using a non-dimensional index called leakiness (Le). Leakiness (Le) is defined as the ratio of the volumetric flow rate of fluid that is leaked through the inter-bristle gaps in the direction opposite to wing motion under viscous (realistic) conditions to the volumetric flow rate for inviscid conditions, and is given by the equation:

$$Le = \frac{Q_{\text{viscous}}}{Q_{\text{inviscid}}} \tag{10}$$

where Q_{viscous} represents the volumetric flow rate leaked through the bristles under viscous condition calculated from the 2D PL-PIV measurements alog wing span, Q_{inviscid} represents the volumetric flow rate leaked through the bristles under no viscous resistance (inviscid flow) calculated based on the assumption that under no viscous resistance, all the flow leaks through the inter-bristle gap (Kasoju et al. 2018).

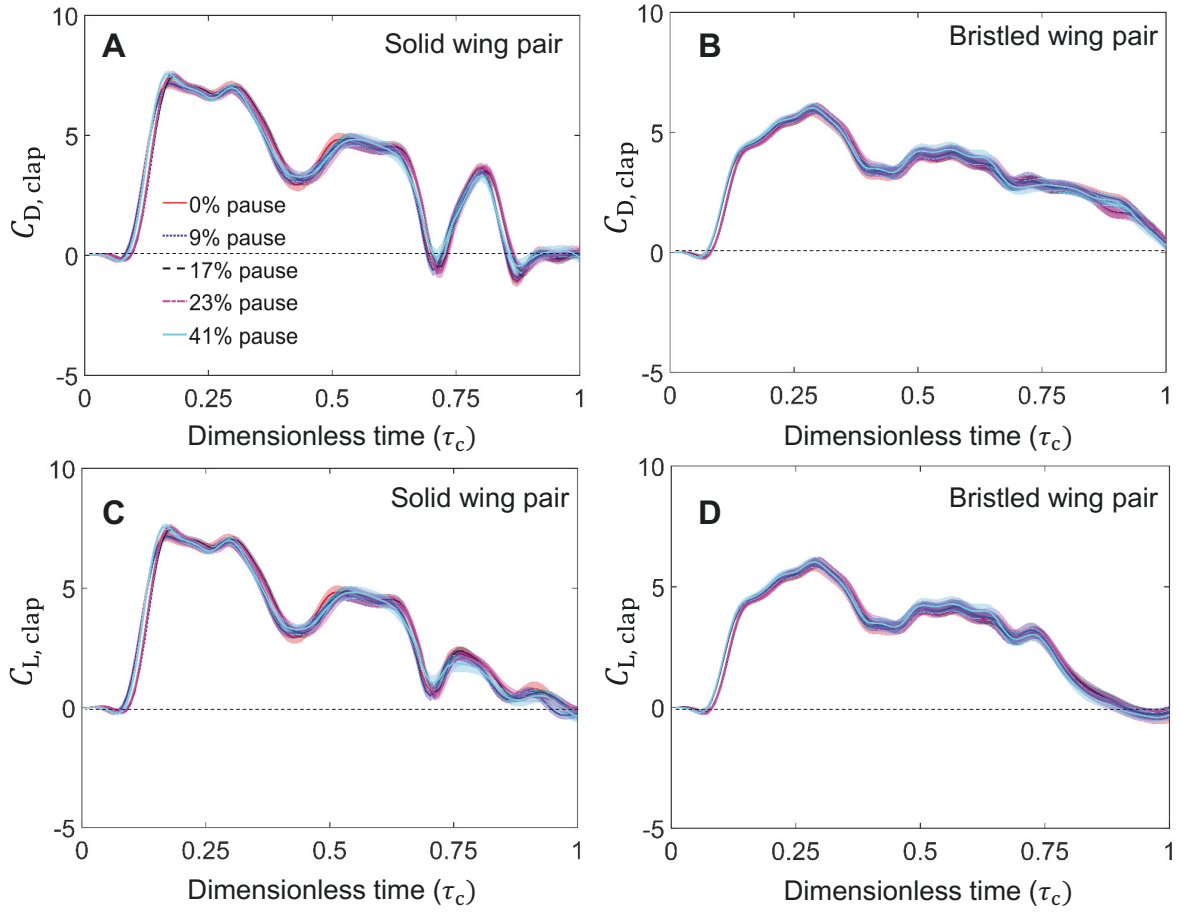

Figure 4. Force coefficients during upstroke (clap stroke) for a wing pair at Re_c=10 with shading around each curve representing range of ±1 standard deviation for that particular data (across 30 cycles). (A) and (C) show the drag coefficient (C_{D}) and lift coefficient (C_{L}), respectively, during upstroke (clap stroke) (τ_{c}) for the solid wing pair at various pause times. (B) and (D) show the drag coefficient (C_{D}) and lift coefficient (C_{L}), respectively, during upstroke (clap stroke) (τ_{c}) for the bristled wing pair at various pause times.

3. Results

3.1. Force generation

Single wing during upstroke (clap stroke). For a single wing in upstroke (clap stroke) phase, both lift (C_{L}) and drag (C_{D}) coefficients (Figure 3) were found to increase during early stages of clap, where the wing was made to accelerate during translation. Both the solid and bristled wing models were found to show little variation in force generation (C_{D} and C_{L}) during constant velocity translation (τ_{c}=0.35-0.7). During the end of upstroke (clap stroke) phase (τ_{c}=0.7-1), we observed both C_{L} and C_{D} to vary significantly in time, with change in direction of force generation. C_{L} and C_{D} for the single bristled wing were found to be lower compared to those of the single solid wing throughout the entire upstroke (clap stroke) phase. Interestingly, C_{D} did not reach zero at the end of upstroke (clap stroke) phase when the wings come to rest. This was presumably due to the wing wake not dissipating completely. Changing the pause time, which occurs after upstroke (clap stroke) phase, produced no significant variation in forces generated during the upstroke (clap stroke) phase.

Wing pair during upstroke (clap stroke). For the solid and bristled wing pair in upstroke (clap stroke) phase, the trends for C_{L} and C_{D} (Figure 4) are consistent with previously published data on solid and bristled wings (Santhanakrishnan et al. 2014, Kasoju et al. 2018, Ford et al. 2019). Starting from rest, the two wing-pairs were made to rotate and translate towards each other showing an increase in force coefficients in the initial acceleration phase. This is followed by constant velocity wing translation (τ_{c}=0.35-0.7), where both solid and bristled wing were found to show little variation in force generation (C_{D} and C_{L}) in time. During the end of upstroke (clap stroke) phase (τ_{c} = 0.7-1), we observed the drag coefficient (C_{D}) to vary significantly in time for the solid wing (Figure 4A) compared to the bristled wing (Figure 4B). This was presumably due to wing-wing interaction, as the wings approach close to each other at the end of upstroke (clap stroke) phase. However, lift coefficients (C_{L}) for both solid and bristled wings (Figure 4C,D) were found to drop during the end of upstroke (clap stroke) phase. Similar to the single wing, changing the pause time produced no variation in force generated during the upstroke (clap stroke) phase (occurring before the pause). Unlike the single wing, we observed both C_{L} and C_{D} to reach zero towards the end of upstroke (clap stroke) when the wings come to rest.

Single wing during downstroke (fling stroke). For a single wing (solid and bristled), C_{D} was found to peak during early stages of downstroke (fling stroke) (Figure 5A,B), where the wings were accelerating when performing rotation and translation. For both the solid and bristled wing, C_{D} mostly remained constant during constant velocity translation and decreased during deceleration. Peak drag coefficient for the solid wing was noticeably higher compared to the bristled wing. Varying pause time, which occurred before the start of fling, showed little to no variation in C_{D} for both the solid and bristled wings. Thus, pausing after upstroke (clap stroke) does not impact drag force generation on a single wing in downstroke (fling stroke).

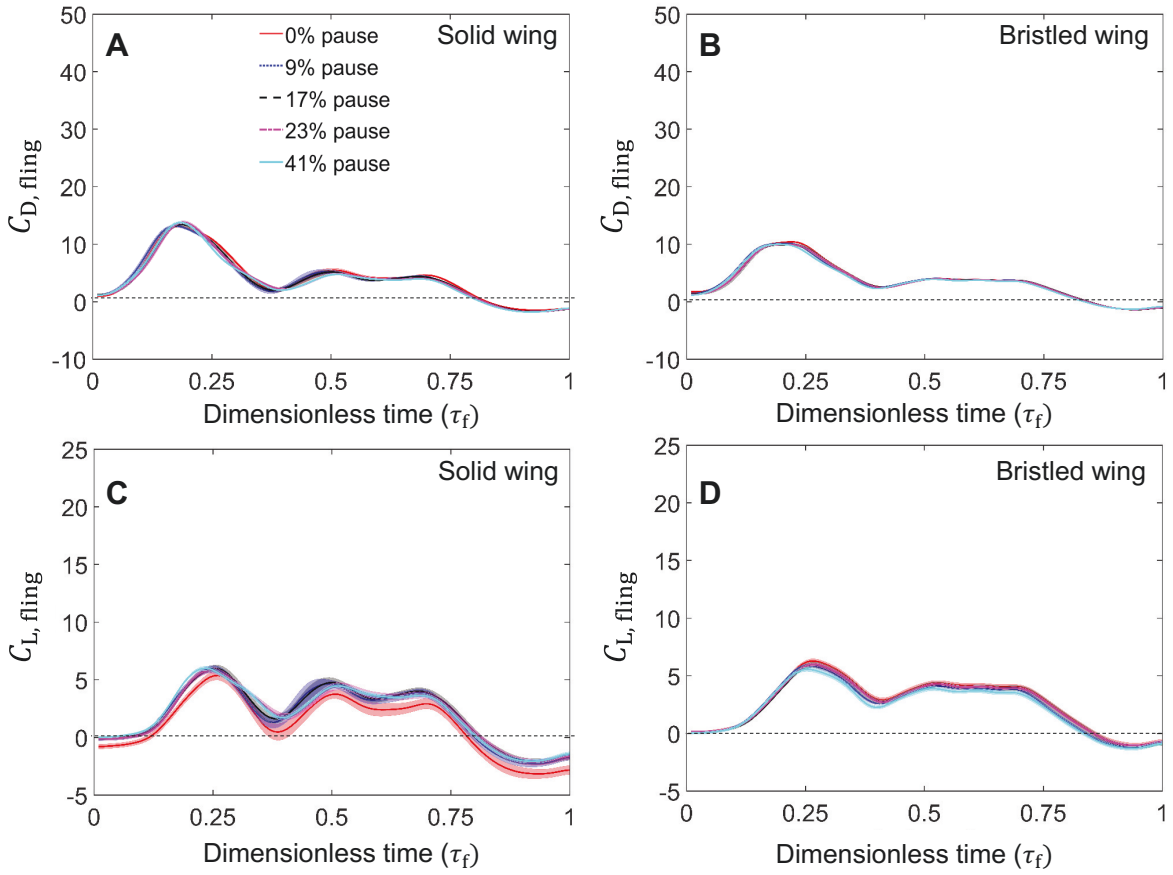

Figure 5. Force coefficients during downstroke (fling stroke) for a single wing at Re_c=10 with shading around each curve representing range of ±1 standard deviation for that particular data (across 30 cycles). (A) and (C) show the drag coefficient (C_D) and lift coefficient (C_L), respectively, during downstroke (fling stroke) (τ_f) for the solid wing model at various pause times. (B) and (D) show the drag coefficient (C_D) and lift coefficient (C_L), respectively, during downstroke (fling stroke) (τ_f) for the bristled wing model at various pause times.

In contrast to C_D, pausing the solid wing before the start of downstroke (fling stroke) resulted in noticeably changing C_L as compared to 0% pause condition (Figure 5C). C_L for a single solid wing (Figure 5C) was found to significantly vary during the entire downstroke (fling stroke) phase, with peak C_L occurring during early downstroke (fling stroke). Towards the end of downstroke (fling stroke) phase, we observed noticeable negative C_L owing to wing deceleration at a high angle of attack. C_L for a single bristled wing (Figure 5D) was found to significantly vary during the entire downstroke (fling stroke) phase, such that peak C_L occurred during early fling, followed by nearly constant C_L during constant velocity translation and a subsequent drop in C_L towards the end of downstroke (fling stroke) when the wing starts to decelerate. In contrast to the solid wing, varying pause time for the single bristled wing resulted in no variation in C_L throughout the downstroke (fling stroke) phase.

Wing pair during downstroke (fling stroke). C_D was observed to peak during

early stages of downstroke (fling stroke) for both solid and bristled wings (Figure 6A,B), where the wings were accelerating when performing rotation and translation. This tremendous increase in drag coefficient during early stages of downstroke (fling stroke) was presumably due to wing-wing interaction. Interestingly, drag coefficients were found to drop for the rest of the downstroke (fling stroke) phase, when the wings moved farther apart. This clearly indicates the influence of wing-wing interaction on drag coefficient, and was also observed in several previous studies (Miller & Peskin 2004, Miller & Peskin 2005, Arora et al. 2014, Santhanakrishnan et al. 2014, Jones et al. 2016, Kasoju et al. 2018, Ford et al. 2019). Peak C_{D} for the bristled wing during downstroke (fling stroke) was significantly lower compared to the solid wing for any test condition tested in this study (Figure 6A,B). Increasing the percentage of pause time before the start of downstroke (fling stroke) showed little drop in C_{D}. Unlike the single wing during downstroke (fling stroke) (Figure 5B), increasing the pause time produced a more noticeable effect on drag force generation in two-winged downstroke (fling stroke).

Similar to C_{D}, C_{L} for both solid and bristled wings (Figure 6C,D) were found to peak in the early stages of downstroke (fling stroke), showing the influence of wing-wing interaction. C_{L} was subsequently found to mostly remain constant and then drop during constant velocity translation and deceleration of the wing, respectively. Towards the end of downstroke (fling stroke) phase, both C_{L} and C_{D} were found to change their direction owing to wing deceleration. Similar to C_{D}, influence of changes in pause time were noticeable for C_{L} during downstroke (fling stroke). Similar to the single solid wing during downstroke (fling stroke, Figure 5C), the solid wing pair showed noticeable change in C_{L} with varying pause time.

Single wing and wing pair during pause. Both C_{D} and C_{L} were found to remain constant throughout the pause period (see Figures S1-S2 in supplementary material). For a single wing (both solid and bristled), C_{D} was constant and positive-valued during the pause period. By contrast, C_{D} was found to be close to zero during the pause period of a wing pair (both solid and bristled wings; see Figure S1 in supplementary material). Irrespective of percentage of pause time, C_{L} was found to be close to zero during the entire pause period (see Figure S2 in supplementary material). In addition to non-dimensional force plots presented in supplementary material (Figures S1-S2), dimensional drag forces (F_{D}) and dimensional lift forces (F_{L}) for the entire cycle are provided in the supplementary material in Figure S3 and Figure S4, respectively. The time-varying trends in dimensional forces (F_{L}, F_{D}) for a given condition (i.e., varying pause time for solid/bristled wing; solid/bristled wing pair) were unchanged compared to dimensionless force coefficients (C_{L}, C_{D}) for the same condition.

Phase-averaged force coefficients. To obtain an overall understanding of the changes in force coefficients with pause time in between upstroke (clap stroke) and downstroke (fling stroke) phase, we examined the magnitudes of phase-averaged force coefficients during upstroke (clap stroke, $\overline{C_{\mathrm{D,clap}}}$ and $\overline{C_{\mathrm{L,clap}}}$) and downstroke (fling stroke), $\overline{C_{\mathrm{D,fling}}}$ and $\overline{C_{\mathrm{L,fling}}}$) separately (Figure 7 and 8).

We first discuss findings on a single wing shown in Figure 7. Changes in pause

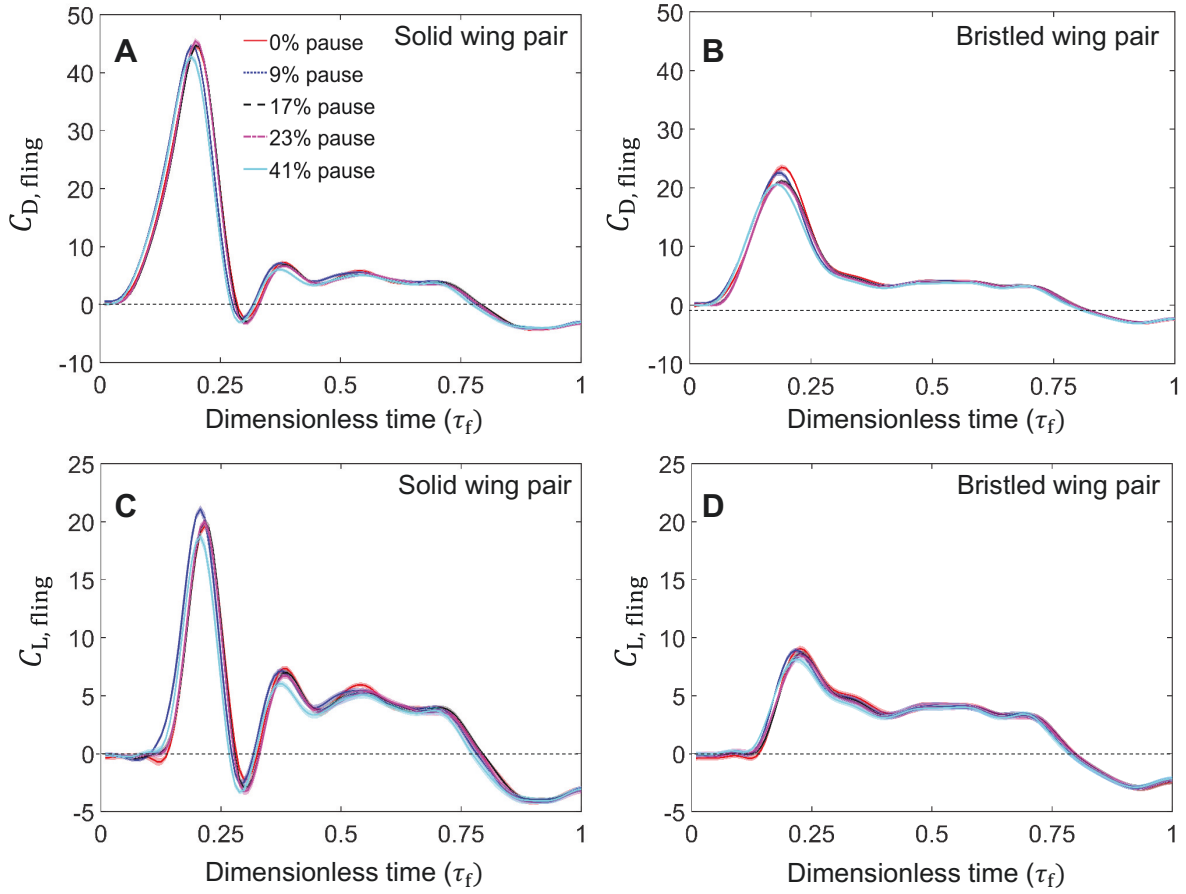

Figure 6. Force coefficients during downstroke (fling stroke) for a wing pair at Re_c=10 with shading around each curve representing range of ±1 standard deviation for that particular data (across 30 cycles). (A) and (C) show the drag coefficient (C_D) and lift coefficient (C_L), respectively, during downstroke (fling stroke) (τ_f) for the solid wing pair at various pause times. (B) and (D) show the drag coefficient (C_D) and lift coefficient (C_L), respectively, during downstroke (fling stroke) (τ_f) for the bristled wing pair at various pause times.

time showed no influence on phase-averaged force coefficients ($\overline{C_{D,clap}}$ and $\overline{C_{L,clap}}$) for both the solid and bristled wings (Figure 7A,B) during clap. Interestingly, the values of $\overline{C_{D,clap}}$ and $\overline{C_{L,clap}}$ for both solid and bristled wings were almost similar with bristled wing having lower values of $\overline{C_{D,clap}}$ and $\overline{C_{L,clap}}$ compared to solid wing. Also, due to significant negative drag (C_D) observed towards the end of upstroke (clap stroke) for a single wing configuration (solid and bristled), the phase-averaged drag coefficient ($\overline{C_{D,clap}}$) was found to be significantly decrease and $\overline{C_{D,clap}}$ was found to be noticeably lower compared to $\overline{C_{L,clap}}$ (Figure 7A). During downstroke (fling stroke, Figure 7C,D), changes in pause time also showed little to no influence on $\overline{C_{D,fling}}$ for both the solid and bristled wings. However, $\overline{C_{L,fling}}$ for the single solid wing was found to increase with increasing pause time. While, $\overline{C_{L,fling}}$ was found to increase from 0% pause to 9% pause and then showed no influence with increasing pause time. Similar to clap, the values

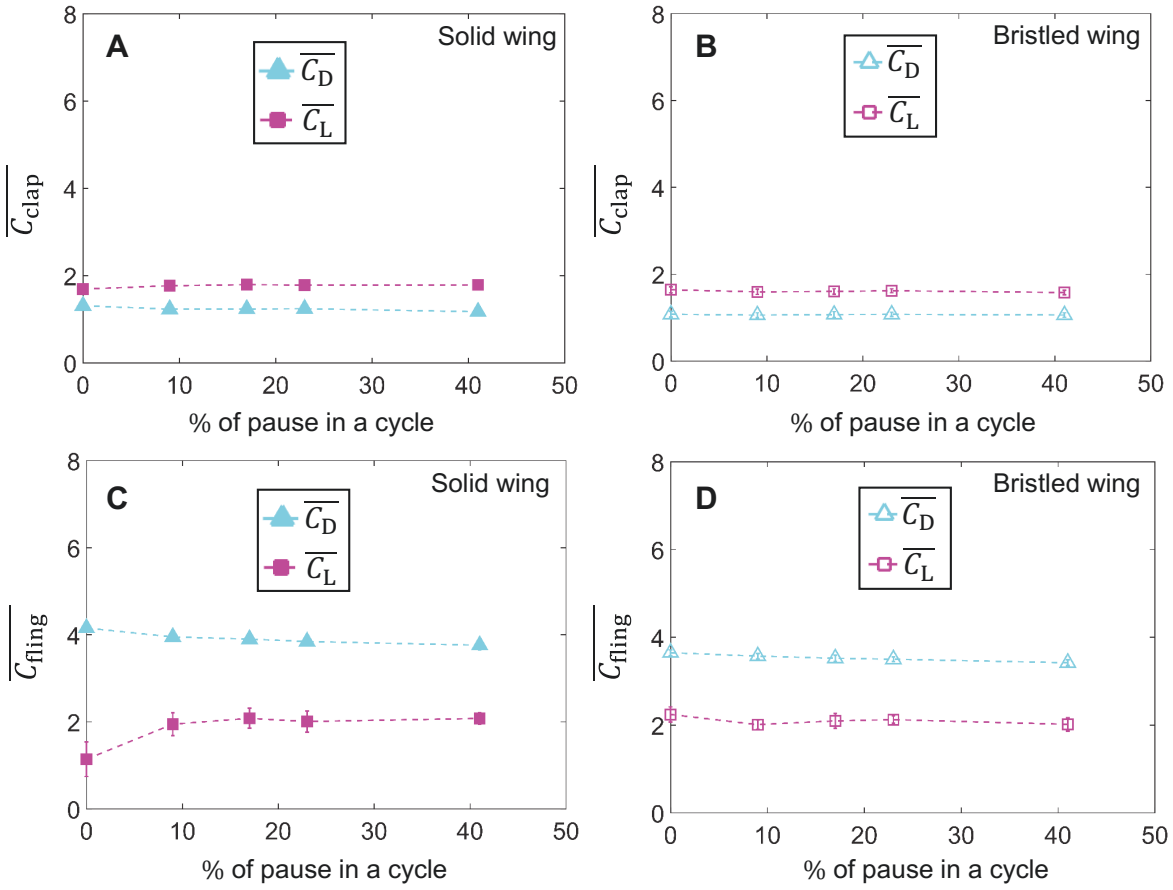

Figure 7. Magnitudes of phase-averaged force coefficients during upstroke (clap stroke) and downstroke (fling stroke) for a single wing at Re_c=10, presented separately for each phase with error bars representing ±1 standard deviation for that particular data (across 30 cycles). (A) and (B) show the phase-averaged drag coefficient ($\overline{C_D}$) and phase-averaged lift coefficient ($\overline{C_L}$) for varying pause times during upstroke (clap stroke) for the solid and bristled wing models, respectively. (C) and (D) show $\overline{C_D}$ and $\overline{C_L}$ for varying pause times during downstroke (fling stroke) for the solid and bristled wing models, respectively. Solid markers represents solid wing model, hollow markers represents bristled wing model.

of $\overline{C_{D,fling}}$ for the solid and bristled wings were almost similar across all pause times. Interestingly, $\overline{C_{L,fling}}$ for the bristled wing was found to be a little more or similar to that of the solid wing for all the percentages of pause time. We suspect this could be due to the added mass affect during varying wing motion (rotation and translation) affecting a solid wing (Kasoju et al. 2018, Chin & Lentink 2016, Daniel 1984) dominantly as compared to a bristled wing.

We next discuss phase-averaged force coefficients on wing pairs as shown in Figure 8. Changes in pause time showed no influence on phase-averaged force coefficients during upstroke (clap stroke, $\overline{C_{D,clap}}$ and $\overline{C_{L,clap}}$) for both the solid and bristled wing pairs (Figure 8A,B). Similar to the single solid wing (Figure 7A,B), the values of $\overline{C_{D,clap}}$ and $\overline{C_{L,clap}}$ for both the solid and bristled wing pairs were almost similar. For

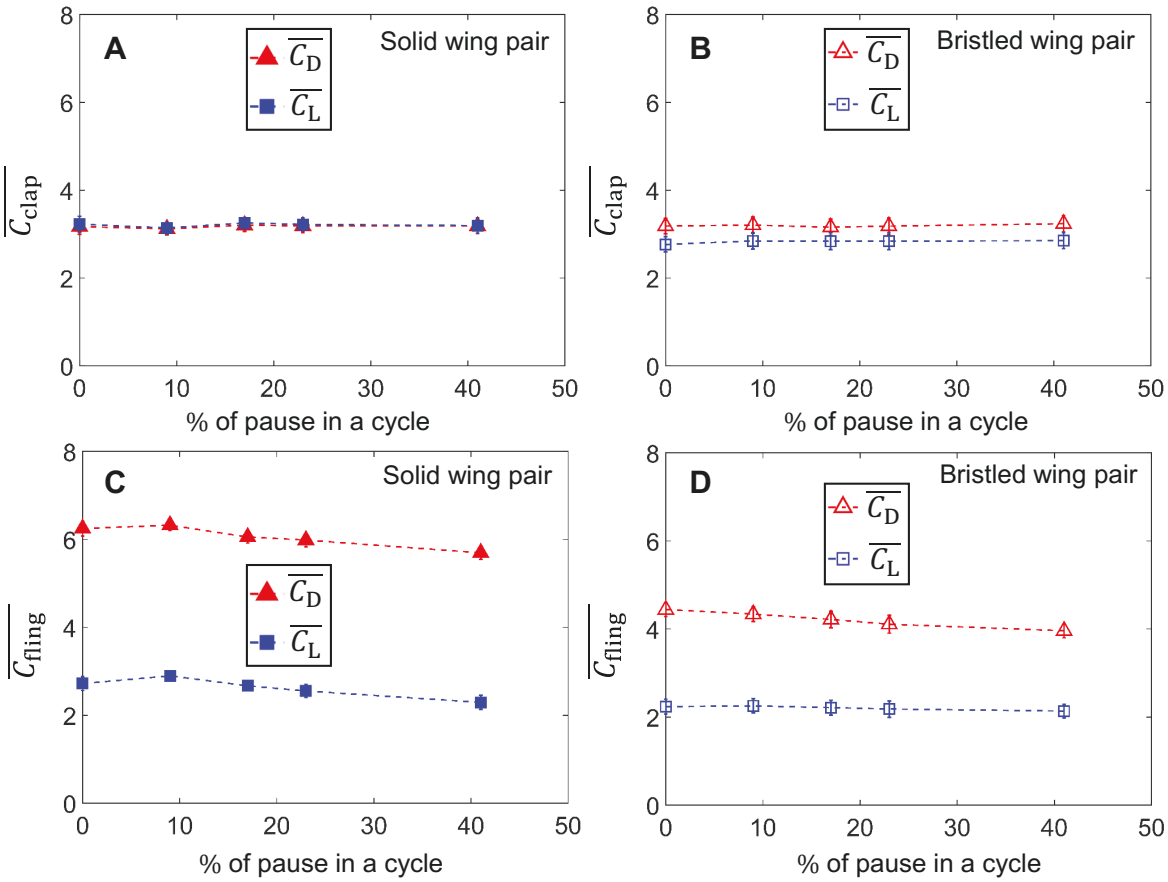

Figure 8. Magnitudes of phase-averaged force coefficients during upstroke (clap stroke) and downstroke (fling stroke) for wing pair at Re_c=10, presented separately for each phase with error bars representing ±1 standard deviation for that particular data (across 30 cycles). (A) and (B) show the phase-averaged drag coefficient ($\overline{C_D}$) and phase-averaged lift coefficient ($\overline{C_L}$) for varying pause times during upstroke (clap stroke) for the solid and bristled wing pair, respectively. (C) and (D) show $\overline{C_D}$ and $\overline{C_L}$ for varying pause times during downstroke (fling stroke) for the solid and bristled wing pairs, respectively. Solid markers represents solid wing model, hollow markers represents bristled wing model.

the solid wing pair during downstroke (fling stroke, Figure 8C), increasing pause time decreased $\overline{C_{D,fling}}$ and $\overline{C_{L,fling}}$ noticeably. For the bristled wing pair during downstroke (fling stroke, Figure 8D), increasing pause time showed small decrease in $\overline{C_{D,fling}}$, while there was no variation in $\overline{C_{L,fling}}$. $\overline{C_{D,fling}}$ for the solid wing pair was greater than $\overline{C_{D,fling}}$ of the bristled wing pair across all pause times. In addition, $\overline{C_{L,fling}}$ showed little variation between the solid and bristled wing pairs at all pause times.

3.2. Chordwise flow fields

Phase-averaged force coefficients ($\overline{C_D}$ and $\overline{C_L}$) showed little to no variation between solid and bristled wing models during upstroke (clap stroke) for both the single wing and wing pair configurations, and the flow structures were also essentially similar when comparing

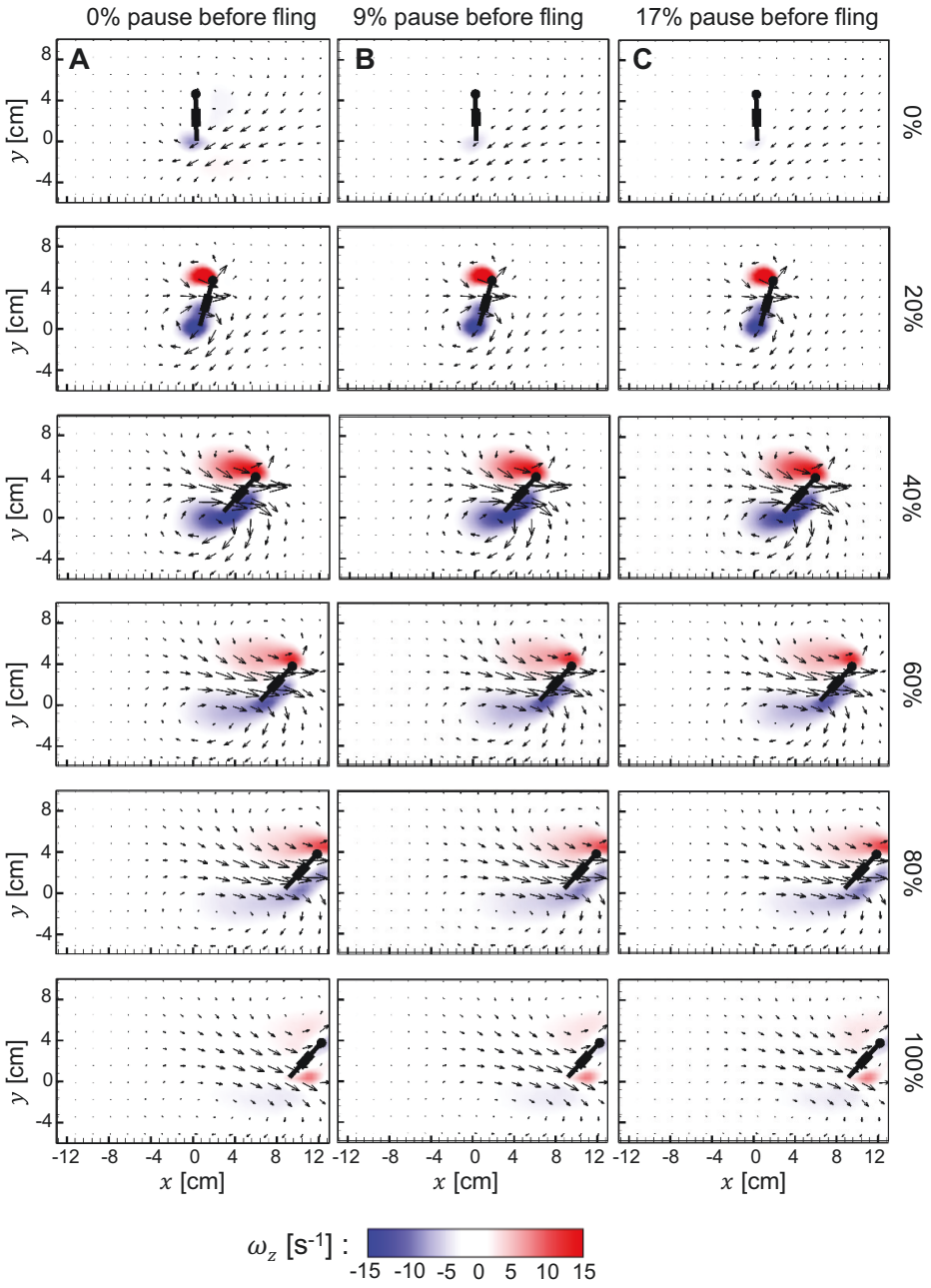

Figure 9. Velocity vector fields overlaid on out-of-plane z-vorticity (ω_z) contours for the single bristled wing during downstroke (fling stroke) at Re_c=10 for various pause times: (A) 0%, (B) 9%, (C) 17% of cycle time. For each pause condition, 6 timepoints (0%, 20%, 40%, 60%, 8-% and 100% of downstroke (fling stroke) time) are shown along each column (increasing time from top to bottom). Red colour represents counterclockwise vorticity, while blue represents clockwise vorticity.

the solid and bristled wing models. The flow structures around solid wing pair during upstroke (clap stroke) were similar to those observed in our previous study (Kasoju et al. 2018) and are thus not shown here. Also, the flow structures for the single solid wing during upstroke (clap stroke) were similar in trend to that of the solid wing pair but with different vortex strengths.

Similar to clap, flow around a single wing (or a wing pair) during downstroke (fling stroke) showed identical trends when comparing solid and bristled wings (or wing pairs). Both the LEV and TEV were found to increase in strength during early stages of downstroke (fling stroke, Figures 9-10) and later found to decrease in strength, with vorticity being diffused into the fluid medium surrounding the wing. The strength of the LEV and TEV of the single bristled wing in downstroke (fling stroke) was less than or similar to that of the bristled wing pair. Interestingly, just before the start of downstroke (fling stroke) for 0% pause case, we observed the formation of a wake with low vorticity in the fluid medium surrounding the wing (for both the single wing and wing pair configurations). This was most likely remnant of the wake generated from the upstroke (clap stroke) phase that was just completed.

3.3. LEV and TEV circulation

Single wing during upstroke (clap stroke). We examined the strength of the flow structures by calculating LEV circulation (Γ_{LEV}) and TEV circulation (Γ_{TEV}) of the single wing models (solid and bristled) during upstroke (clap stroke, Figure 11A,B) and during downstroke (fling stroke, Figure 11C,D). Both Γ_{LEV} and Γ_{TEV} followed the same trend in time during upstroke (clap stroke) (except towards the end) when comparing solid (Figure 11A) and bristled (Figure 11B) wings. Near the end of clap, Γ_{LEV} of the single solid wing dropped close to zero unlike that of the single bristled wing. The magnitude of Γ_{LEV} during upstroke (clap stroke) for the single bristled wing model was slightly lower as compared to that of the solid wing. However, the magnitude of Γ_{TEV} during upstroke (clap stroke) for the single bristled wing was similar to that of the solid wing. Therefore, we can expect that the net circulation (i.e., $|\Gamma_{\mathrm{LEV}}|$-$|\Gamma_{\mathrm{TEV}}|$) for the solid wing would be a little greater than that of the bristled wing. These circulation results are in agreement with the larger lift generation during upstroke (clap stroke) for the single solid wing (Figure 3C) as compared to the single bristled wing (Figure 3D). Changing the pause time showed no variation in Γ_{LEV} and Γ_{TEV} during upstroke (clap stroke) for both the solid and bristled wings.

Single wing during downstroke (fling stroke). Γ_{LEV} and Γ_{TEV} for both the solid and bristled wings were found to increase during early stages of fling, remain constant during constant velocity translation and later decrease in time during wing deceleration (Figure 11C,D). Compared to the solid wing, both Γ_{LEV} and Γ_{TEV} were lowered in the bristled wing. With increasing pause time, Γ_{LEV} for both the solid and bristled wings were found to marginally decrease while Γ_{TEV} was unchanged. The net circulation over the wing (i.e., $|\Gamma_{\mathrm{LEV}}| - |\Gamma_{\mathrm{TEV}}|$) is thus expected to marginally decrease with

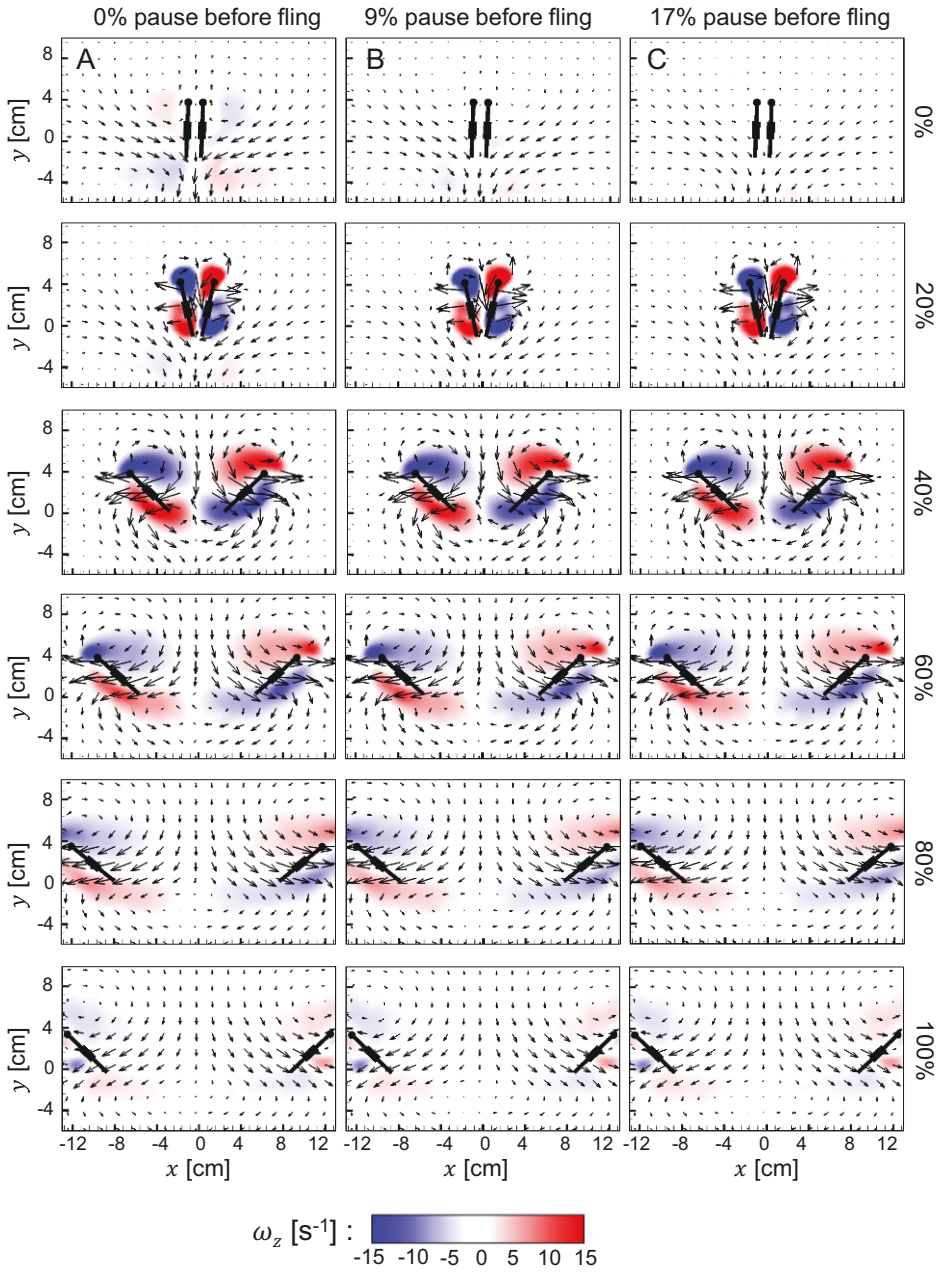

Figure 10. Velocity vector fields overlaid on out-of-plane z-vorticity (ω_z) contours for the bristled wing pair during downstroke (fling stroke) at Re_c=10 for various pause times: (A) 0%, (B) 9%, (C) 17% of cycle time. For each pause condition, 6 timepoints (0%, 20%, 40%, 60%, 8-% and 100% of downstroke (fling stroke) time) are shown along each column (increasing time from top to bottom). Red colour represents counterclockwise vorticity, while blue represents clockwise vorticity.

increasing pause time in both the solid and bristled wing models. This is in disagreement with the observed lift generation during downstroke (fling stroke) by a single solid wing (Figure 5C), where increasing pause duration beyond 0% resulted in moderately increasing C_{L}. Increasing pause time did not alter $C_{\mathrm{L,fling}}$ of a single bristled wing (Figure 5D), which is also in disagreement with the marginal decrease expected in net circulation of the single bristled wing with increasing pause time. These discrepancies suggest that additional lift generation mechanisms (added mass effects, delayed stall) need to be considered during downstroke (fling stroke) (as opposed to circulatory lift) in both solid and bristled wing models.

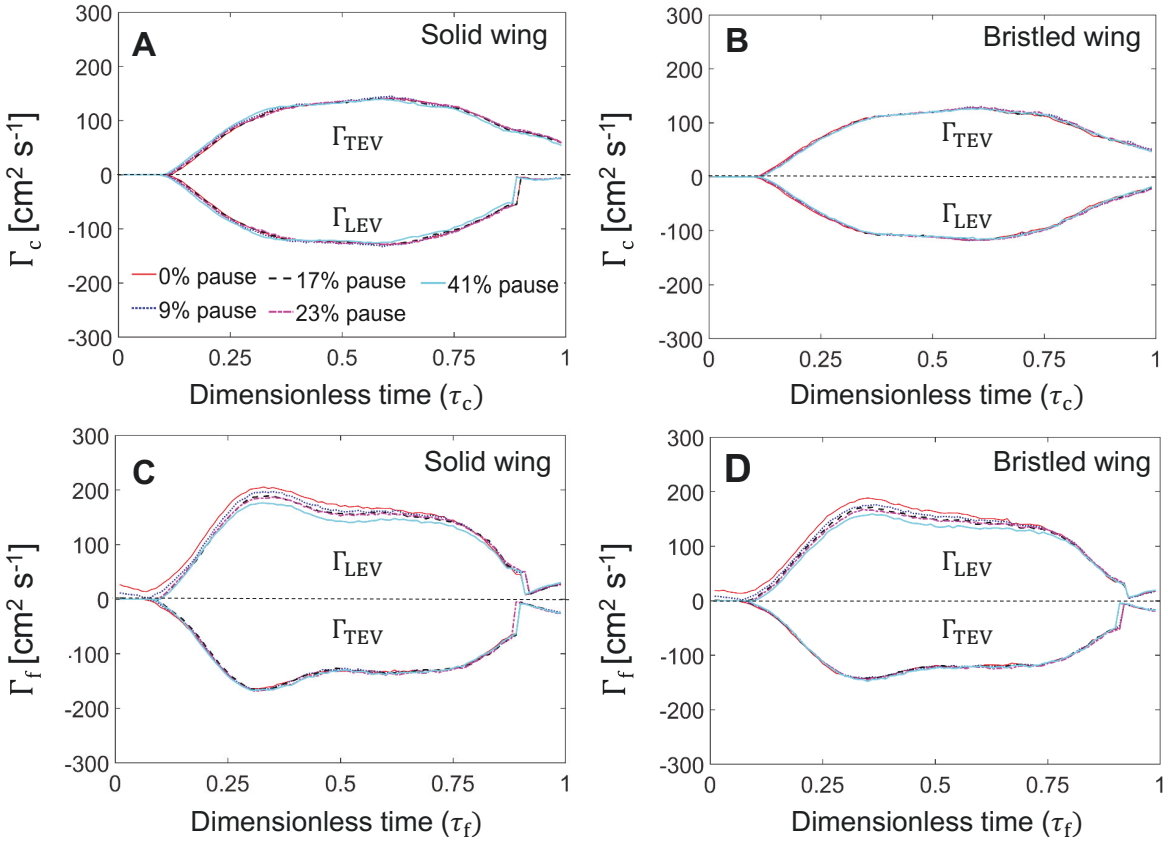

Figure 11. LEV AND TEV circulation of a single wing as a function of dimensionless time. (A) and (C) show circulation of the solid wing during upstroke (clap stroke) and fling, respectively. (B) and (D) show circulation of the bristled wing during upstroke (clap stroke) and fling, respectively.

Wing pair during upstroke (clap stroke). Both Γ_{LEV} and Γ_{TEV} of the solid wing pair (Figure 12A) and the bristled wing pair (Figure 12B) followed the same time-varying trend during upstroke (clap stroke) as the corresponding trends of a single wing during upstroke (clap stroke, Figure 11A,B). In addition, the magnitudes of Γ_{LEV} and Γ_{TEV} of the bristled wing pair during upstroke (clap stroke, Figure 12B) were lower compared to those of the solid wing pair (Figure 12A). This is expected to reduce the lift generated by the bristled wing pair, which is in agreement with the observed lift

generation during upstroke (clap stroke, Figure 4C,D). An interesting point to note is that in contrast to the single wing during upstroke (clap stroke, Figure 11A,B), both Γ_{LEV} and Γ_{TEV} of wing pairs (Figure 12A,B) were found to peak later in the upstroke (clap stroke) phase when the wings come in close proximity of each other (i.e., during wing-wing interaction). Overall, changing the pause time resulted in no variation in Γ_{LEV} and Γ_{TEV} during upstroke (clap stroke) of a wing pair (solid or bristled). This is in agreement with the lack of variation of $C_{\mathrm{L,clap}}$ with pause time (Figure 4C,D).

Wing pair during downstroke (fling stroke). For the solid wing pair in fling, Γ_{LEV} and Γ_{TEV} were found to steeply increase and decrease in time during early downstroke (fling stroke, Figure 12C). While for the bristled wing pair, a gradual increase and decrease in both Γ_{LEV} and Γ_{TEV} was observed in early downstroke (fling stroke, Figure 12D). Γ_{LEV} and Γ_{TEV} for the bristled wing pair (Figure 12D) followed a similar trend to that of the single bristled wing (Figure 11D). The magnitudes of Γ_{LEV} and Γ_{TEV} during downstroke (fling stroke) were lower for the bristled wing pair as compared to those of the solid wing pair, which is expected to reduce the lift generated by the bristled wing pair. This is in agreement with the observed lift generation during downstroke (fling stroke) of a wing pair (Figure 6C,D). With increasing pause time, we observed little to no variation in Γ_{LEV} and Γ_{TEV} throughout downstroke (fling stroke). This 'non-effect' of pause time on circulation in downstroke (fling stroke) is not in agreement with the previously observed decrease in C_{L} with increasing pause time by a wing pair during downstroke (fling stroke, Figure 6C,D). Similar to the discrepancies noted earlier in comparison of net circulation and lift generation of a single wing in fling, circulatory lift cannot adequately account for small changes in lift generation. Non-circulatory lift mechanisms such as added mass effects, delayed stall and pressure distribution around the wing need to be considered to fully explain lift generation of a wing pair during fling, as has been noted in our recent study (Kasoju & Santhanakrishnan 2021).

3.4. Leakiness

Fluid leakage through the gaps between the bristles was characterized from 2D PL-PIV measurements using leakiness (Le) defined in equation (10). Since drag reduction was significantly higher for the bristled wing pair during downstroke (fling stroke) as compared to the single bristled wing during fling, we only examined Le of the bristled wing pair during downstroke (fling stroke, Figure 13). Across all pause times, we observed Le to increase during early stages of fling, remain constant during constant velocity translation and then decrease during deceleration. This trend of Le variation in time was similar to the time variation of C_{D} of the bristled wing pair in downstroke (fling stroke, Figure 6B). Peak Le occurred in early downstroke (fling stroke) at τ_{f}=0.25, and decreased with increasing pause time from 0% to 23%. Interestingly, peak $C_{\mathrm{D,fling}}$ also decreased with increasing pause time (Figure 6B). Though it is intuitive to expect that C_{D} must decrease with increase in Le, this discrepancy suggests that Le is not the major

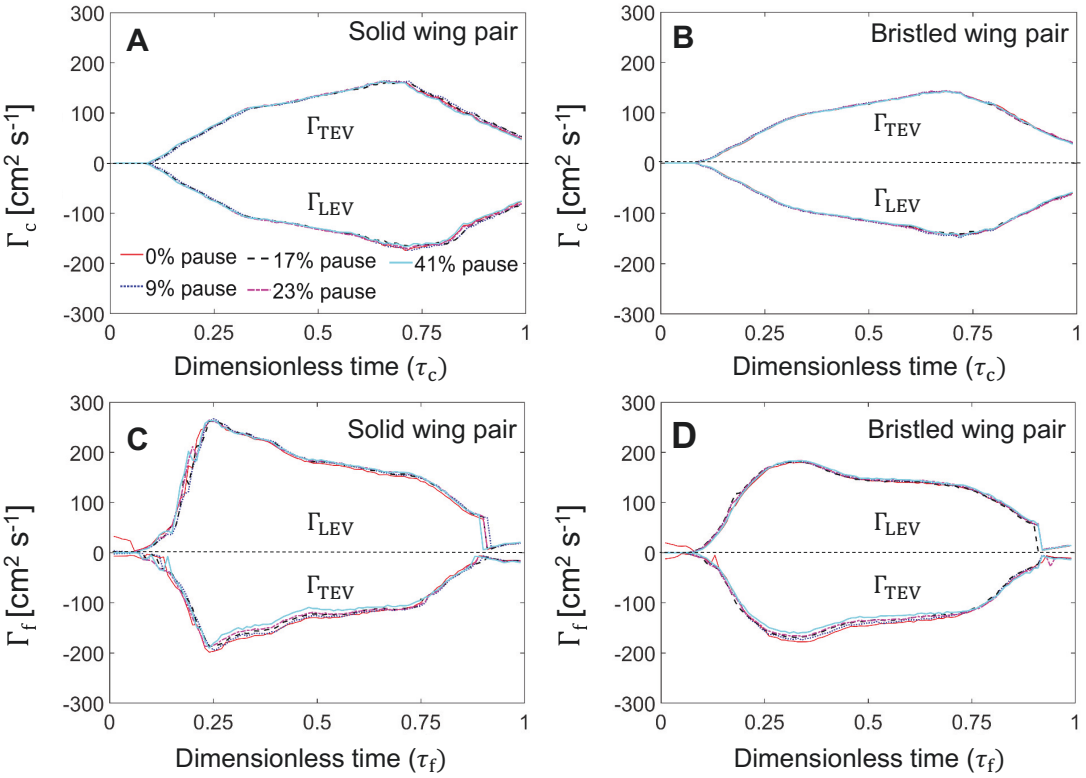

Figure 12. LEV AND TEV circulation of a wing pair as a function of dimensionless time. (A) and (C) show circulation of the solid wing pair during upstroke (clap stroke) and fling, respectively. (B) and (D) show circulation of the bristled wing pair during upstroke (clap stroke) and fling, respectively.

mechanism underlying peak C_D reduction with increasing pause time in the bristled wing pair during downstroke (fling stroke). We expect that pressure distribution over each wing of the bristled wing pair (Kasoju & Santhanakrishnan 2021) would decrease with increasing pause time, thereby decreasing both Le and C_D simultaneously.

3.5. Power requirement

To examine the amount of power required by a wing to overcome the drag generated when performing upstroke (clap stroke) and downstroke (fling stroke) motion, we calculated the power coefficient (C_P) for each pause duration from the single wing and wing pair force measurements (solid and bristled wings) using equation (7). The time-variation of C_P throughout a cycle, including clap, pause and downstroke (fling stroke) phases, is shown in the supplementary material (Figure S5). For both solid and bristled wing models, peak C_P for the single wing was significantly lower compared to that of the wing pair, ostensibly on account of wing-wing interaction in the latter configuration. Similarly, C_P of the bristled wing was significantly lower compared to that of the solid wing in both the single wing and wing pair configurations. This was expected due to reduction in C_D during upstroke (clap stroke, Figure 3B; Figure 4B) and downstroke

(fling stroke, Figure 5B; Figure 6B) by the bristled wing models as compared to solid wing models (Figure 3A; Figure 4A) and downstroke (fling stroke, Figure 5A; Figure 6A). As expected based on C_{D} during upstroke (clap stroke, Figure 3A,B; Figure 4A,B), changing pause time resulted in no impact on peak C_{P} during upstroke (clap stroke) phase for a given wing design (solid or bristled) and wing configuration (single wing or wing pair). For the single wing as well as the wing pair (solid or bristled), peak C_{P} during downstroke (fling stroke) decreased with increasing pause time (see Figure S5 in supplementary material). Peak C_{P} decrease during downstroke (fling stroke) with increasing pause time was more pronounced for wing pair configuration as compared to the single wing (solid or bristled), as expected from C_{D} for a wing pair in downstroke (fling stroke, see insensitivity to pause time for single wings in Figure 5A,B compared to wing pairs in Figure 6A,B).

4. Discussion

Using a dynamically scaled robotic platform to execute upstroke (clap stroke) and downstroke (fling stroke) kinematics in physical wing models, we measured aerodynamic forces and performed flow visualization on single wings and wing pairs (solid and bristled) with a pause duration following upstroke (clap stroke) and before the start of downstroke (fling stroke) at Re_c=10. The major results of this study are: 1) including a pause after the upstroke (clap stroke) phase does not impact magnitudes of phase-averaged force coefficients ($\overline{C_{\mathrm{L}}}$, $\overline{C_{\mathrm{D}}}$) and flow structures (i.e., Γ_{LEV}, Γ_{TEV}) generated during the upstroke (clap stroke) phase, irrespective of wing design (solid or bristled) and wing configuration (single wing or wing pair); 2) increasing pause time lowers peak force coefficients (C_{L},C_{D}), phase-averaged force coefficients ($\overline{C_{\mathrm{L}}}$, $\overline{C_{\mathrm{D}}}$) and peak power coefficient (C_{P}) during fling; and 3) aerodynamic effects of including a pause after the upstroke (clap stroke) phase are minimal in a single wing (solid or bristled) as compared to a wing pair (solid or bristled). Collectively, these findings show that wing-wing interaction observed in flapping flight of tiny insects is necessary to realize any aerodynamic benefit (i.e., decreasing C_{D}, C_{P}) of pausing between upstroke (clap stroke) and downstroke (fling stroke).

Based on the high-speed video sequences of *E. Formosa* during hovering (Cheng & Sun 2018) and forward flight (Cheng & Sun 2021), we determined that these wasps pause for about 0.2 ms to 0.4 ms (estimated from "Top View" video sequences from 0.8 ms to 1.2 ms in Cheng & Sun (2021)) before the start of downstroke (fling stroke). For an estimated cycle time of 2.8 ms, the pause duration of *E. formosa* is in the range of 7%-14% of their cycle. This range of pause duration is close to the range reported in our manuscript and by Ellington (1975). Further analyzing the high-speed video sequences of thrips (*Frankliniella occidentalis*) (Lyu et al. 2019), we observed close to 8% pause between upstroke (clap stroke) and downstroke (fling stroke) from 3 flapping cycles. Collectively, these separate data sets show that multiple species of tiny flying insects tend to pause their wing motion before the start of downstroke (fling stroke). However,

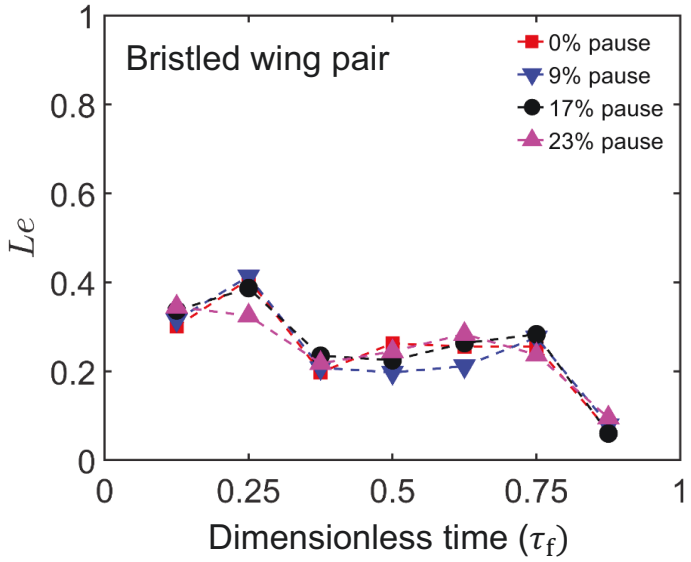

Figure 13. Leakiness (Le), representing non-dimensional flow reduction by a bristled wing during wing-wing interaction of the bristled wing pair, as a function of downstroke (fling stroke) time (τ_f).

the influence of pause time on aerodynamic force generation have not been examined in previous studies of upstroke (clap stroke) and downstroke (fling stroke) at low Re_c (Miller & Peskin 2004, Kasoju et al. 2018, Arora et al. 2014, Ford et al. 2019). In this study, a bristled wing model with total surface area equal to 33% of a geometrically similar solid wing area was tested. This drop in surface area of the wing should directly decrease the force generated by bristled wings. However, irrespective of pause time, the magnitudes of phase-averaged force coefficients during clap ($\overline{C_{\mathrm{D,clap}}}$ and $\overline{C_{\mathrm{L,clap}}}$) for a solid wing were almost similar to that of bristled wing in both the single wing and wing pair configurations (Figure 7A,B; Figure 8A,B). We suspect that this close similarity in forces between the solid and bristled wings during clap is due to the blockage effect that is caused by the shear layers around the bristles at lower G/D ratios, as described in previous studies (Lee & Kim 2017, Kasoju et al. 2018). This phenomenon causes the inter-bristle gap to be blocked due to shear layers formed around each bristle, thereby not allowing the fluid to pass through the gaps in between the bristles. This forces the fluid to move around the bristled wing (Davidi & Weihs 2012), thereby generating forces that are mostly equivalent to a solid wing model. Furthermore, this similarity between the solid and bristled wing during the upstroke (clap stroke) phase (both single wing and wing pair configurations) was also evident in the circulation plots, where both $\Gamma_{\mathrm{c,LEV}}$ and $\Gamma_{\mathrm{c,TEV}}$ were almost similar between the solid wing and bristled wings (Figure 11A,B; Figure 12A,B).

In contrast to the upstroke (clap stroke) phase, phase-averaged lift coefficient during downstroke (fling stroke, $\overline{C_{\mathrm{L,fling}}}$) at 0% pause was noticeably different between the solid and bristled wing models in both single wing (Figure 7C,D) and wing pairs

(Figure 8C,D). With increasing pause time, $\overline{C_{\mathrm{L,fling}}}$ of solid and bristled wings became similar in both the single wing and the wing pair configurations. In contrast to $\overline{C_{\mathrm{L,fling}}}$, phase-averaged drag coefficient in downstroke (fling stroke, $\overline{C_{\mathrm{D,fling}}}$) was essentially unchanged when comparing the single solid wing (Figure 7C) to the single bristled wing (Figure 7D) at a given pause time. However, $\overline{C_{\mathrm{D,fling}}}$ noticeably decreased for both bristled wing pair (Figure 8D) and solid wing pair (Figure 8C). Further examination of the bristled wing pair during downstroke (fling stroke) showed that there was a 44% drop in peak C_{D} relative to that of the solid wing pair (from Figure 6A,B) at 0% pause time. Interestingly, investigating the flow through the bristles using 2D PL-PIV and characterizing the leakiness (Le), we found that the peak leakiness was about 40% (Figure 13), which is similar to drop in peak C_{D} of the bristled wing pair relative to the solid wing pair during downstroke (fling stroke) phase. We therefore conclude that leakiness is responsible for the observed drop in C_{D} during downstroke (fling stroke) for the bristled wing pair.

From the Figure 7C and Figure 8C, we can see that during downstroke (fling stroke) at 0% pause time, phase-averaged drag coefficient ($\overline{C_{\mathrm{D}}}$) of the solid wing pair was 50% greater than $\overline{C_{\mathrm{D}}}$ of the single solid wing, while phase-averaged lift coefficient ($\overline{C_{\mathrm{L}}}$) of the solid wing pair was 138% greater than $\overline{C_{\mathrm{L}}}$ of the single solid wing. During downstroke (fling stroke) for non-zero pause times, $\overline{C_{\mathrm{D}}}$ of the solid wing pair was 50-60% greater than $\overline{C_{\mathrm{D}}}$ of the single solid wing, and $\overline{C_{\mathrm{L}}}$ of the solid wing pair was 10-50% greater than $\overline{C_{\mathrm{L}}}$ of the single solid wing. During upstroke (clap stroke) at 0% pause time (Figure 7A, Figure 8A), we observed $\overline{C_{\mathrm{D}}}$ and $\overline{C_{\mathrm{L}}}$ of the solid wing pair were 142% and 92% greater than those of the single solid wing, respectively. For non-zero pause times during upstroke (clap stroke), $\overline{C_{\mathrm{D}}}$ of the solid wing pair was 153-172% greater than $\overline{C_{\mathrm{D}}}$ of the single solid wing; and $\overline{C_{\mathrm{L}}}$ of the single solid wing pair was 77-79% greater than $\overline{C_{\mathrm{L}}}$ of the single solid wing.

We compared our solid wing findings to those reported by Miller & Peskin (2005) for similar wing kinematics and Reynolds number. Miller & Peskin (2005) considered 50% overlap between rotation and start of translation, which was lower than the 100% overlap considered in this study. They reported 10%-40% increase in average lift coefficient of a solid wing pair compared to that of a single solid wing during downstroke (fling stroke). Subsequent studies (Arora et al. 2014, Kasoju & Santhanakrishnan 2021) have shown that increasing the overlap between rotation and start of translation of a solid wing pair increases average force coefficients during downstroke (fling stroke). We also observed larger increase in negative lift coefficient ($C_{\mathrm{L,fling}}$) during downstroke (fling stroke) of the single solid wing for 0% pause time as compared to other pause times (Figure 5C). This large negative C_{L} contributed to a significant drop in $\overline{C_{\mathrm{L}}}$ of the single solid wing for 0% pause time. The cause of negative lift is likely due to added mass effects experienced during wing deceleration toward the end of downstroke (fling stroke). Surprisingly, Miller & Peskin (2005) did not see any negative lift during end of downstroke (fling stroke) for both solid wing pair and single solid wing. It is important to note that whereas Miller & Peskin (2005) performed 2D numerical simulations, the flow

generated by our test facility was allowed to propagate in three-dimensions. We expect that the use of 100% overlap, negative lift generation and three-dimensionality of the flow field collectively contributed to the observed differences in $\overline{C_{\mathrm{L}}}$ during downstroke (fling stroke) as compared to those reported by Miller & Peskin (2005).

In contrast to downstroke (fling stroke), Miller & Peskin (2005) observed negative lift coefficients ($C_{\mathrm{L,clap}}$) being generated during upstroke (clap stroke) by both a solid wing pair and a single solid wing. However, we observed little to no negative $C_{\mathrm{L,clap}}$ (Figure 3C,Figure 4C) during upstroke (clap stroke). This is likely due to Miller & Peskin (2005) prescribing wing rotation to start towards the end of upstroke (clap stroke) unlike the combined rotation and translation (i.e., 100% overlap) used in the present study.

Unlike the lift coefficient, Miller & Peskin (2005) observed drag coefficient (C_{D}) to remain positive during the entire upstroke (clap stroke) and downstroke (fling stroke) for both a solid wing pair and a single solid wing. However, we observed C_{D} to become negative during both upstroke (clap stroke) and downstroke (fling stroke) for both solid wing pair and single solid wing. As explained earlier when comparing C_{L}, differences in C_{D} between our study and those reported by Miller & Peskin (2005) can also be attributed to our use of 100% overlap in rotation and linear translation, added mass effects and three-dimensionality of the flow generated by the experimental test facility.

Similar to the single solid wing, we observed drag coefficients to become negative for the single bristled wing (Figure 3B, Figure 3D) towards the end of upstroke (clap stroke). However, we observed marginal to no negative lift for the single bristled wing during the end of upstroke (clap stroke). We suspect that this noticeable change in sign for drag coefficients is due to wing deceleration with varying angle of attack, which can contribute to significant added mass effect on the wings (Chin & Lentink 2016). The contribution of added mass effects in driving lift force coefficient to negative for single bristled wing were likely minimal. Compared to the single solid wing, C_{L} and C_{D} for both the solid wing pair and the bristled wing pair performing upstroke (clap stroke, Figure 4) did not show noticeable negative values. This difference between the single wing and wing pair configurations suggests that added mass effects can be dampened by the opposing motion of the two wings of a wing pair. Similar to the upstroke (clap stroke), forces changed in sign during deceleration in the downstroke (fling stroke) of single wing models (both solid and bristled, Figure 5) and wing pairs (solid wing pair and bristled wing pair, Figure 6). Wing-wing interaction is negligible during deceleration of the solid wing pair or bristled wing pair, as the wings are farther apart. Across both the upstroke and downstroke, we can therefore conclude that wing-wing interaction decreases the contribution of added mass effects on both the single wing and wing pair models.

4.1. Implications of varying pause time on cycle-averaged and peak coefficients

Figure 14A,B shows cycle-averaged coefficients ($\overline{C_{\mathrm{L,net}}}$ and $\overline{C_{\mathrm{D,net}}}$) for the entire cycle

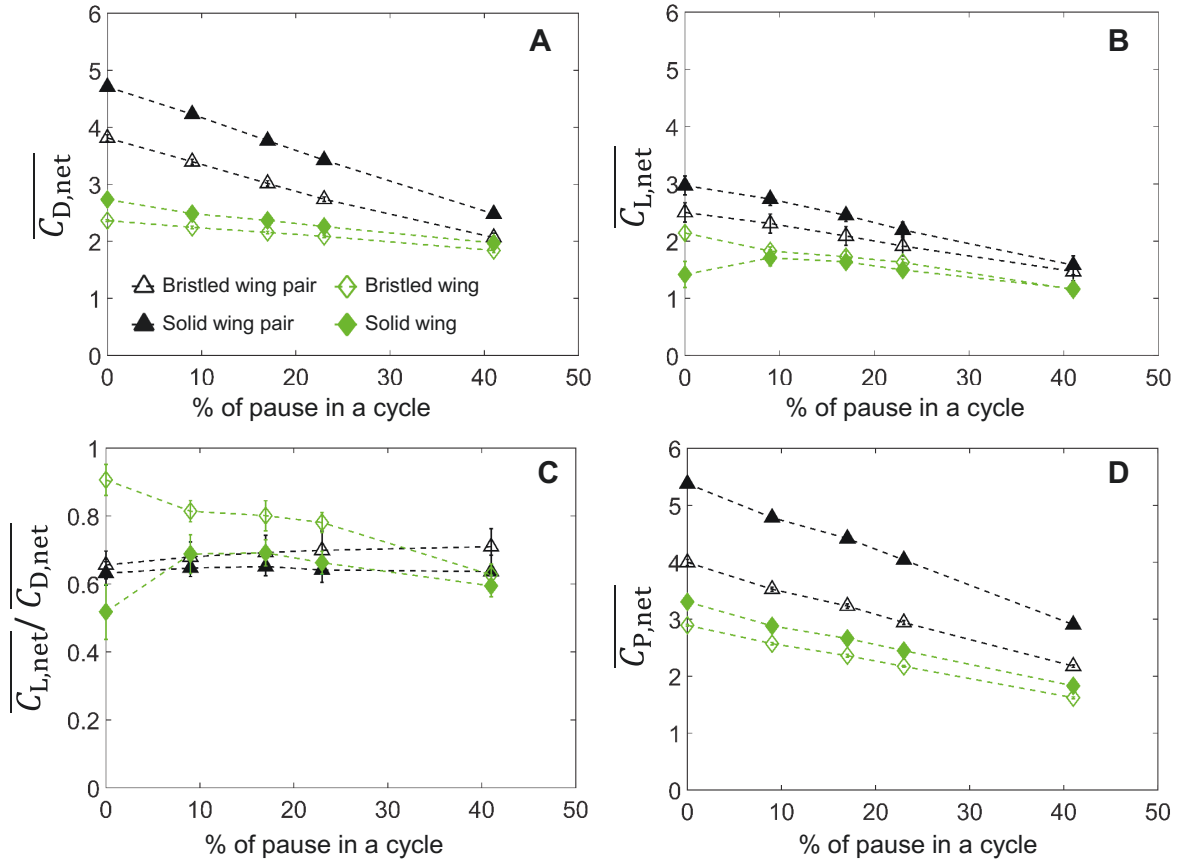

Figure 14. (A,B) Cycle-averaged net force coefficients ($\overline{C_{\mathrm{D,net}}}$, $\overline{C_{\mathrm{L,net}}}$), (C) ratio of cycle-averaged net lift over cycle-averaged net drag ($\overline{C_{\mathrm{L,net}}}/\overline{C_{\mathrm{D,net}}}$), and (D) Cycle-averaged net power coefficient ($\overline{C_{\mathrm{P,net}}}$) calculated over the entire cycle (upstroke (clap stroke) phase, pause time and downstroke (fling stroke) phase) across varying pause times. Legend is shown in part A. Solid markers represents solid wing model, hollow markers represents bristled wing model.

(including upstroke (clap stroke) time, pause time and downstroke (fling stroke) time). Increase in pause time increases the entire cycle time. With increasing pause time, $\overline{C_{\mathrm{D,net}}}$ was found to decrease for both the solid wing pair and the bristled wing pair. By contrast, $\overline{C_{\mathrm{D,net}}}$ showed little variation with increasing pause time in both the single solid wing and the single bristled wing. With increasing pause time, $\overline{C_{\mathrm{L,net}}}$ was found to decrease for both single wing and wing pair configuration. With increasing duration of pause time, $\overline{C_{\mathrm{L,net}}}$ of the solid wing was found to reach values close to that of the bristled wing in both the single wing and wing pair configurations (Figure 14A,B). Therefore, a significant reduction in cycle-averaged net force generation occurs with increasing pause time among wing pairs performing wing-wing interaction unlike a single wing (solid or bristled) where wing-wing interaction is absent. It must also be noted that while pausing for longer reduces $\overline{C_{\mathrm{D,net}}}$, there is a compromise associated with simultaneous reduction in $\overline{C_{\mathrm{L,net}}}$—i.e., a tiny insect would inevitably need to expend more energy to regain its vertical position with a longer pause.

Further examining the cycle-averaged drag force coefficients ($\overline{C_{\mathrm{D,net}}}$, Figure 14A), we observed $\overline{C_{\mathrm{D,net}}}$ for wing pair models (solid and bristled) to decrease at a faster rate with increasing pause time in comparison to $\overline{C_{\mathrm{D,net}}}$ variation with pause time for single wing models (solid and bristled). This reduction in the rate of decrease in $\overline{C_{\mathrm{D,net}}}$ with increasing pause time for single wing models is due to non-zero drag coefficients (C_{D}) for the single wing during the pause period (Figure S1). In contrast to the single wing (both solid and bristled), we observed almost zero C_{D} for both solid and bristled wing pair during pause period. This suggests that wing-wing interaction acts like a dampener.

We examined the cycle-averaged net lift to cycle-averaged net drag ratio ($\overline{C_{\mathrm{L,net}}}/\overline{C_{\mathrm{D,net}}}$, Figure 14C) as a measure of aerodynamic efficiency. We observed that the aerodynamic efficiency of solid and bristled wing pairs were essentially invariant with changing pause time (Figure 14C). However, for the single bristled wing case, we observed $\overline{C_{\mathrm{L,net}}}/\overline{C_{\mathrm{D,net}}}$ to decrease with increasing pause time. For the single solid wing, $\overline{C_{\mathrm{L,net}}}/\overline{C_{\mathrm{D,net}}}$ was found to increase and then decrease with increasing pause time. These results potentially suggest that tiny insects that tend to pause their wing motion between upstroke (clap stroke) and downstroke (fling stroke) need not compromise their aerodynamic efficiency when doing so.

Ellington (1975) hypothesized that including a pause before the start of downstroke (fling stroke) could help the insects in elastic storage of high mechanical energy that would be needed to downstroke (fling stroke) the wings apart. Although elastic storage of energy in flight has not been examined for tiny insects such as thrips, a previous study by Dickinson & Lighton (1995) presented clear evidence that fruit flies need elastic mechanisms for efficient flight. Another study by Alexander (1995) suggested that wing muscles of many insects can function as springs and store energy for reuse in the next flapping stroke. Another means to achieve efficient flight is to have effective muscle efficiency, which requires larger metabolic energy consumption. It remains unknown at present as to whether thrips use elastic storage.

If we were to assume there is no elastic storage, tiny insects such as thrips require large muscle power to overcome severe viscous drag during the start of downstroke (fling stroke) or during braking. A non-dimensional estimate of the power required to overcome the drag (C_{P}) is presented in supplementary material (Figure S5). While C_{P} did not vary with pause time during upstroke (clap stroke) for a given wing design and wing configuration, C_{P} decreased with increasing pause time during fling for both single wing and wing pair configurations. C_{P} was lower for the bristled wing and the bristled wing pair as compared to the equivalent configuration of the solid wings. In addition, increasing the pause time resulted in a larger decrease of the cycle-averaged net power coefficient ($\overline{C_{\mathrm{P,net}}}$, Figure 14D) for the wing pair configurations as compared to the single wing configurations. Pausing effectively lowers the power required to clap wings together and fling them apart in both the solid and bristled wing pairs. A significant drop in $\overline{C_{\mathrm{P,net}}}$ was observed for the bristled wing pair (as compared to the solid wing pair) at 0% pause time compared to 41% pause time. Therefore, bristled wing pairs benefit from larger power reduction at lower pause times.

To support the above comparisons made using statistically estimated (i.e., cycle-averaged) $\overline{C_{\mathrm{L,net}}}$, $\overline{C_{\mathrm{D,net}}}$ and $\overline{C_{\mathrm{P,net}}}$, we examined peak values of force and power coefficients (Figure 15) extracted from instantaneous measurements of C_{L} and C_{D} (Figures 3-6), and direct calculations of time-varying C_{P} from instantaneous C_{D} using equation (7) provided in the supplementary material (Figure S5). The peak values were extracted from C_{L}, C_{D}, C_{P} across the entire cycle consisting of upstroke (clap stroke) phase, pause and downstroke (fling stroke) phase. For a single wing (solid or bristled), we observed essentially no variation in peak drag coefficient ($C_{\mathrm{D,max}}$, Figure 15A) and peak lift coefficient ($C_{\mathrm{L,max}}$, Figure 15B) with increasing pause time. Irrespective of pause time, $C_{\mathrm{D,max}}$ for the single solid wing was slightly greater than that of the single bristled wing. However, $C_{\mathrm{L,max}}$ did not show variation between the single solid wing and the single bristled wing across all pause times. In contrast to the single wing configuration, we observed $C_{\mathrm{D,max}}$ to decrease (by 4%-13%) with increasing pause time for the bristled wing pair. The largest reduction of $C_{\mathrm{D,max}}$ for the bristled wing pair occurred at 17% pause time, and increasing the pause time further did not alter $C_{\mathrm{D,max}}$. Compared to $C_{\mathrm{D,max}}$, we observed smaller reduction (by 1%-10%) of $C_{\mathrm{L,max}}$ for the bristled wing pair with increasing pause time (Figure 15B). For the solid wing pair, increasing the pause time resulted in little to no variation of both $C_{\mathrm{D,max}}$ and $C_{\mathrm{L,max}}$. For a given pause time, $C_{\mathrm{D,max}}$ of the solid wing pair was significantly higher than the bristled wing pair. Compared to $C_{\mathrm{D,max}}$ reduction between the solid and bristled wing pairs, $C_{\mathrm{L,max}}$ reduction by the bristled wing pair (as compared to the solid wing pair) was significantly lower (Figure 15B). Overall, these observations are in agreement with results of previous studies (Kasoju et al. 2018, Ford et al. 2019) that have shown wing-wing interaction using bristled wings to provide larger drag reduction and smaller lift reduction when compared to solid wings.

For a single solid wing, $C_{\mathrm{P,max}}$ increased slightly with increasing pause time (Figure 15C). $C_{\mathrm{P,max}}$ showed little to no variation with increasing pause time for a single bristled wing. With increasing pause time, $C_{\mathrm{P,max}}$ for the bristled wing pair was significantly lowered (by 7%-17%) as compared to the corresponding reduction of $C_{\mathrm{P,max}}$ of the solid wing pair (by 4%-8%). When collectively comparing both the single wing and wing pair configurations, the bristled wing pair provided the largest $C_{\mathrm{P,max}}$ reduction with increasing pause time along with a small reduction in $C_{\mathrm{L,max}}$.

From the biological standpoint, tiny insects such as thrips show the obligatory use of wing-wing interaction during free flight (Lehmann et al. 2005). This strategy has been associated with increased lift generation in a challenging flow regime where viscous dissipation of kinetic energy is significant (Sane 2003, Miller & Peskin 2009, Sane 2016). However, large drag forces are required to fling the wings apart at low Re_c (Miller & Peskin 2005). Bristled wing structure characteristic of insects flying at this Re_c have been reported in several studies to offer beneficial drag reduction (Santhanakrishnan et al. 2014, Jones et al. 2016, Kasoju et al. 2018, Ford et al. 2019). However, far less is known as to how specific aspects of the wingbeat kinematics can further benefit flight at this low Re_c. Despite evidence of a pause incorporated at the end of upstroke

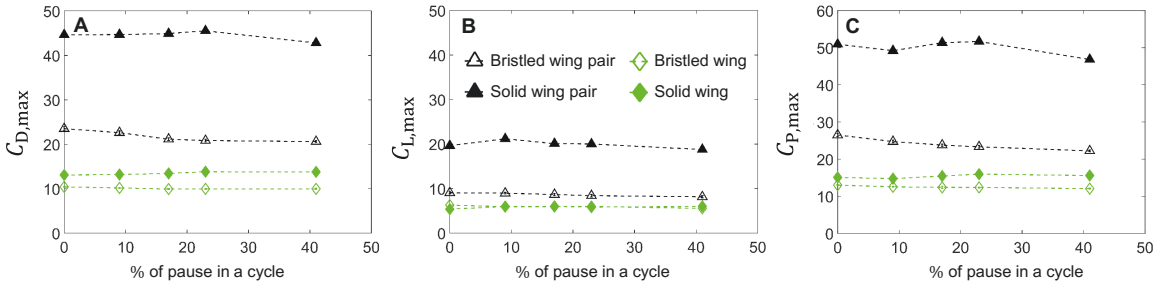

Figure 15. (A,B) Peak force coefficients ($C_{\mathrm{D,max}}$, $C_{\mathrm{L,max}}$) and (C) peak power coefficient ($C_{\mathrm{P,max}}$) calculated over the entire cycle (upstroke (clap stroke) phase, pause time and downstroke (fling stroke) phase) across varying pause times. Legend is shown in part B. Solid markers represents solid wing model, hollow markers represents bristled wing model.

(clap stroke) phase in *E. formosa* (Ellington 1975) and in thrips (current study), the aerodynamic effects of including a pause between upstroke (clap stroke) and downstroke (fling stroke) have not been previously examined. We find that in addition to increase in lift force generation with wing-wing interaction, including a pause between the upstroke (clap stroke) and downstroke (fling stroke) phases can decrease the power required by reducing both cycle-averaged and peak drag coefficients (Figure 14D, Figure 15C). Arguably, using large pause times between upstroke (clap stroke) and downstroke (fling stroke) would be more beneficial by reducing the required power. However, increasing the pause time is also associated with reduction of the cycle-averaged net lift coefficient (Figure 14B), and peak lift coefficient (Figure 15B). Opting for a small pause period (∼10% of cycle) between upstroke (clap stroke) and fling, as observed in the free take-off flight of thrips in this study, can be beneficial in reducing power consumption with a small compromise in lift force generation.

4.2. Implications of varying pause time on flow generation

From 2D TR-PIV flow fields in the chordwise direction (Figure 9, Figure 10), we observed the formation of a wake with low vorticity in the fluid medium surrounding the wing (for both single bristled wing and bristled wing pair) just before the start of fling for 0% pause case. This was most likely a remnant of the wake generated from the upstroke (clap stroke) that was just completed. However, this wake was found to diminish for pause time of 9% and greater than 9%. We expect that waiting until the wake vorticity is fully diminished could decrease the drag forces acting on the wing which would further decrease the power requirement.

For bristled wing pair during downstroke (fling stroke), we observed a small decrease in phase-averaged drag coefficient ($\overline{C_{\mathrm{D,fling}}}$) with increasing pause time (Figure 8D). However, $\overline{C_{\mathrm{L,fling}}}$ showed no variation with increasing pause time (Figure 8D). Therefore, as the wake diminishes with increasing pause time at the start of downstroke (fling

stroke, Figure 10), drag on the wing was found to decrease with no changes in lift generation. This drop in drag directly relates to drop in power required to fling the wings.

For a solid wing pair, we observed noticeable drop in both $\overline{C_{\mathrm{D,fling}}}$ and $\overline{C_{\mathrm{D,fling}}}$ with increasing pause time (Figure 8C) during downstroke (fling stroke). The chordwise flow field for solid wing pair (see Figure S6 in supplementary material) during downstroke (fling stroke) were similar to that observed in bristled wing pair but with increased vortex strength. Therefore, the drop in phase-averaged force coefficients ($\overline{C_{\mathrm{D,fling}}}$) and ($\overline{C_{\mathrm{L,fling}}}$) is a consequence of the wake diminishing with increasing pause time, which can be directly related to drop in power required to fling the wings (equation 7).

Single bristled wing showed little to no variation in $\overline{C_{\mathrm{D,fling}}}$ and $\overline{C_{\mathrm{L,fling}}}$ with increasing pause time (Figure 7D). The wing wake observed for a single bristled wing at start of downstroke (fling stroke) was significantly lower with a weak clockwise vortex formed at the tip of the trailing edge (Figure 9). Therefore, for a single bristled wing there is no convincing evidence that introducing pause before the start of downstroke (fling stroke) would noticeably reduce the power.

Similar to single bristled wing, single solid wing showed little to no variation in $\overline{C_{\mathrm{D,fling}}}$ with increasing pause time (Figure 7C) during downstroke (fling stroke). While $\overline{C_{\mathrm{L,fling}}}$ was found to increase from 0% pause to 9% pause and then showed no influence with increasing pause time. The chordwise flow field measurements for single solid wing during (see Figure S6 in supplementary material) downstroke (fling stroke) were similar to that observed in single bristled wing but with increased vortex strength. Formation of strong trailing edge vortex with no leading-edge vortex before the start of the downstroke (fling stroke) would significantly drop the lift force. This was also evident from phase-averaged lift coefficient $\overline{C_{\mathrm{L,fling}}}$ plot (Figure 7C). Therefore, for a single solid wing introducing pause before the start of downstroke (fling stroke) showed minimal to no change in $\overline{C_{\mathrm{D,fling}}}$ with small increase in $\overline{C_{\mathrm{L,fling}}}$.

In contrast to downstroke (fling stroke), introducing pause after upstroke (clap stroke) did not show any noticeable changes in either chordwise flow fields or force measurements $\overline{C_{\mathrm{D,clap}}}$ and $\overline{C_{\mathrm{L,clap}}}$ during upstroke (clap stroke) for both single wing and wing pair configurations. Therefore, from the observed flow fields and aerodynamic force analysis measurements, we can confirm that pause after upstroke (clap stroke) can help to reduce the drag force during downstroke (fling stroke) for wing pair configuration and single solid wing, which in turn decreases the power requirement.

4.3. Limitations

It is to be noted that the above results were based on rigid wing models. However, the wings of tiny insects are flexible (Miller & Peskin 2009) and could have the capability to store energy from the wake in the fluid at the end of upstroke (clap stroke) and potentially use this stored energy at the start of downstroke (fling stroke) toward overcoming large drag forces. These hypotheses need to be further investigated with flexible bristled wing models in future studies. In addition, the bristled wings of tiny

insects show broad variation in terms of bristle lengths on either side of the membrane. In this study, we used symmetric bristle lengths because changes to bristle length on each side of the membrane would likely impact aerodynamic force generation. Further, using asymmetric bristle lengths may also lead to three-dimensional flow fields during upstroke (clap stroke) and fling, which are not as well-resolved using planar PIV measurements as in this study. To minimize confounding effects from varying bristle lengths, we used a bristled wing design with equal bristle lengths on each side of the membrane. Further studies need to be conducted to understand the effect of including asymmetric bristle lengths on force generation and flow structures in upstroke (clap stroke) and downstroke (fling stroke).

5. Conclusions

This study showed that pause time between upstroke (clap stroke) and downstroke (fling stroke) has no significant influence on time-varying aerodynamic forces generated during the upstroke (clap stroke) phase (phase before the pause) for both the single wing and wing pair configurations (solid and bristled wing models) at a chord-based Reynolds number of 10. However, we observed variations in time-varying aerodynamic forces with increasing pause time during the downstroke (fling stroke) phase (phase after pause). Considering the force coefficients averaged across the entire cycle (upstroke (clap stroke) phase, pause time, downstroke (fling stroke) phase), both solid and bristled wing pairs were found to provide drag reduction with increasing pause time. Observations of the chordwise flow showed that introducing pause before the start of downstroke (fling stroke) led to the complete dissipation of the wake generated from upstroke (clap stroke). Diminishing the vorticity shed from the upstroke (clap stroke) helped in decreasing the drag force on the wing pair configuration (solid and bristled) during downstroke (fling stroke). With increasing pause time, the cycle-averaged net power coefficient was found to decrease significantly during wing-wing interaction of a wing pair as compared to that of a single wing. Collectively, our findings suggest that pausing before downstroke (fling stroke) can help to reduce the power consumption in clap and fling motion, with a small compromise in lift.

Supplementary Material

See the supplementary material for time courses of: drag coefficient (Figure S1), lift coefficient (Figure S2), dimensional drag force (Figure S3), dimensional lift force (Figure S4) and power coefficient (Figure S5). The velocity vector fields overlaid on top of z-vorticity for single solid wing and solid wing pair is shown in Figure S6. The raw high-speed recordings corresponding to 5 trials listed in Table 1 are available within Figshare Digital Repository: https://doi.org/10.6084/m9.figshare.13053056.

Acknowledgments

The authors would like to thank the following collaborators: Prof. Tyson L. Hedrick (University of North Carolina) for his assistance with acquiring videos of free-flying thrips and providing us generous access to his lab facilities, and Prof. Laura A. Miller (University of Arizona) for her advice on collecting thrips. The authors would also like to thank the following students at Oklahoma State University: Mitchell P. Ford for pointing to Prof. C. P. Ellington's observation on pausing after upstroke (clap stroke) in *E. formosa*, and Truc T. Ngo for her assistance with digitizing thrips flight videos.

Competing interests

The authors declare no financial or otherwise competing interests.

Funding

This research was funded by the National Science Foundation (CBET 1512071 to AS).

References

Alexander, R. M. (1995). Springs for wings, *Science* **268**: 50–51.

Arora, N., Gupta, A., Sanghi, S., Aono, H. & Shyy, W. (2014). Lift-drag and flow structures associated with the "clap and fling" motion, *Phys. Fluids* **26**: 071906.

Birch, J. M., Dickson, W. B. & Dickinson, M. H. (2004). Force production and flow structure of the leading edge vortex on flapping wings at high and low Reynolds numbers, *J. Exp. Biol.* **207**: 1063–1072.

Cheer, A. Y. L. & Koehl, M. A. R. (1987). Paddles and rakes: fluid flow through bristled appendages of small organisms, *J. Theor. Biol.* **129**: 17–39.

Cheng, X. & Sun, M. (2018). Very small insects use novel wing flapping and drag principle to generate the weight-supporting vertical force, *Journal of Fluid Mechanics* **855**: 646–670.

Cheng, X. & Sun, M. (2019). Revisiting the clap-and-fling mechanism in small wasp encarsia formosa using quantitative measurements of the wing motion, *Physics of Fluids* **31**(10): 101903.

Cheng, X. & Sun, M. (2021). Wing kinematics and aerodynamic forces in miniature insect encarsia formosa in forward flight, *Physics of Fluids* **33**(2): 021905.

Chin, D. D. & Lentink, D. (2016). Flapping wing aerodynamics: from insects to vertebrates, *Journal of Experimental Biology* **219**(7): 920–932.

Crespi, B. J., Carmean, D. A. & Chapman, T. W. (1997). Ecology and evolution of galling thrips and their allies, *Annu. Rev. Entomol.* **42**: 51–71.

Daniel, T. L. (1984). Unsteady aspects of aquatic locomotion, *American Zoologist* **24**(1): 121–134.

Davidi, G. & Weihs, D. (2012). Flow around a comb wing in low-Reynolds-number flow, *AIAA J.* **50**: 249–253.

Dickinson, M. H. & Götz, K. G. (1993). Unsteady aerodynamics performance of model wings at low Reynolds numbers, *J. Exp. Biol.* **174**: 45–64.

Dickinson, M. H., Lehmann, F.-O. & Sane, S. P. (1999). Wing rotation and the aerodynamic basis of insect flight, *Science* **284**: 1954–1960.

Dickinson, M. H. & Lighton, J. (1995). Muscle efficiency and elastic storage in the flight motor of Drosophila, *Science* **268**: 87–90.

Ellington, C. (1975). Non-steady-state aerodynamics of the flight of *Encarsia formosa*, *in* T. Y.-T. Wu, C. J. Brokaw & C. Brennen (eds), *Swimming and Flying in Nature: Volume 2*, Springer, Boston, MA, USA, pp. 783–796.

Ellington, C. P. (1999). The novel aerodynamics of insect flight: applications to micro-air vehicles, *J. Exp. Biol.* **202**: 3439–3448.

Ellington, C. P., van den Berg, C., Willmont, A. P. & Thomas, A. L. R. (1996). Leading edge vortices in insect flight, *Nature* **348**: 626–630.

Ford, M. P., Kasoju, V. T., Gaddam, M. G. & Santhanakrishnan, A. (2019). Aerodynamic effects of varying solid surface area of bristled wings performing clap and fling, *Bioinspir. Biomim* **14**: 046003.

Huber, J. T., Gibson, G. A. P., Bauer, L. S., Liu, H. & Gates, M. W. (2008). The genus *mymaromella* (Hymenoptera: Mymarommatidae) in North America, with a key to described extant species, *J. Hymenopt. Res.* **17**: 175–194.

Jalali, S. K., Mohanraj, P. & Lakshmi, B. L. (2016). Trichogrammatids, *in* Omkar (ed.), *Ecofriendly Pest Management for Food Security*, Academic Press, San Diego, CA, USA, chapter 5, pp. 139–181.

Jones, S. K., Yun, Y. J. J., Hedrick, T. L., Griffith, B. E. & Miller, L. A. (2016). Bristles reduce the force required to 'fling' wings apart in the smallest insects, *J. Exp. Biol.* **219**: 3759–3772.

Kasoju, V. T. & Santhanakrishnan, A. (2021). Aerodynamic interaction of bristled wing pairs in fling, *Physics of Fluids* **33**(3): 031901.

Kasoju, V. T., Terrill, C. L., Ford, M. P. & Santhanakrishnan, A. (2018). Leaky flow through simplified physical models of bristled wings of tiny insects during clap and fling, *Fluids* **3**: 44.

Kolomenskiy, D., Moffatt, H. K., Farge, M. & Schneider, K. (2011). The Lighthill–Weis-Fogh clap–fling–sweep mechanism revisited, *J. Fluid Mech.* **676**: 572–606.

Lee, S. H. & Kim, D. (2017). Aerodynamics of a translating comb-like plate inspired by a fairyfly wing, *Phys. Fluids* **29**: 081902.

Lee, S. H., Lahooti, M. & Kim, D. (2018). Aerodynamic characteristics of unsteady gap flow in a bristled wing, *Phys. Fluids* **30**: 071901.

Lee, S. H., Lee, M. & Kim, D. (2020). Optimal configuration of a two-dimensional bristled wing, *J. Fluid Mech.* **888**: A23.

Lehmann, F.-O., Sane, S. P. & Dickinson, M. H. (2005). The aerodynamic effects of wing-wing interaction in flapping insect wings, *J. Exp. Biol.* **208**: 3075–3092.

Liu, H., Ravi, S., Kolomenskiy, D. & Tanaka, H. (2016). Biomechanics and biomimetics in insect-inspired flight systems, *Phil. Trans. R. Soc. B* **371**: 20150390.

Lyu, Y. Z., Zhu, H. J. & Sun, M. (2019). Flapping-mode changes and aerodynamic mechanisms in miniature insects, *Phys. Rev. E* **99**: 012419.

Miller, L. A. & Peskin, C. S. (2004). When vortices stick: an aerodynamic transition in tiny insect flight, *J. Exp. Biol.* **207**: 3073–3088.

Miller, L. A. & Peskin, C. S. (2005). A computational fluid dynamics study of 'clap and fling' in the smallest insects, *J. Exp. Biol.* **208**: 195–212.

Miller, L. A. & Peskin, C. S. (2009). Flexible clap and fling in tiny insect flight, *J. Exp. Biol.* **212**: 3076–3090.

Morse, J. G. & Hoddle, M. (2006). Invasion biol. of thrips, *Annu. Rev. Entomol.* **51**: 67–89.

Riley, D. G., Joseph, S. V., Srinivasan, R. & Diffie, S. (2011). Thrips vectors of tospoviruses, *J. Integr. Pest Manag.* **2**: I1–I10.

Rodriguez-Saona, C. R., Polavarapu, S., Barry, J. D., Polk, D., Jörnsten, R., Oudemans, P. V. & Liburd, O. E. (2010). Color preference, seasonality, spatial distribution and species composition of thrips (Thysanoptera: Thripidae) in northern highbush blueberries, *Crop Protection* **29**: 1331–1340.

Samaee, M., Nelsen, N. H., Gaddam, M. G. & Santhanakrishnan, A. (2020). Diastolic vortex alterations with reducing left ventricular volume: an in vitro study, *J. Biomech. Eng.* **142**(12): 121006.

Sane, S. P. (2003). The aerodynamics of insect flight, *J. Exp. Biol.* **206**: 4191–4208.

Sane, S. P. (2016). Neurobiology and biomechanics of flight in miniature insects, *Curr. Opin. Neurobiol.* **41**: 158–166.

Sane, S. P. & Dickinson, M. H. (2002). The aerodynamic effects of wing rotation and a revised quasi-steady model of flapping flight, *J. Exp. Biol.* **205**: 1087–1096.

Santhanakrishnan, A., Jones, S. K., Dickson, W. B., Peek, M., Kasoju, V. T., Dickinson, M. H. & Miller, L. A. (2018). Flow structure and force generation on flapping wings at low Reynolds numbers relevant to the flight of tiny insects, *Fluids* **3**: 45.

Santhanakrishnan, A., Robinson, A. K., Jones, S., Low, A. A., Gadi, S., Hedrick, T. L. & Miller, L. A. (2014). Clap and fling mechanism with interacting porous wings in tiny insects, *J. Exp. Biol.* **217**: 3898–3909.

Spedding, G. R. & Maxworthy, T. (1986). The generation of circulation and lift in a rigid two-dimensional fling, *J. Fluid Mech.* **165**: 247–272.

Sun, M. & Yu, X. (2006). Aerodynamic force generation in hovering flight in a tiny insect, *AIAA J.* **44**: 1532–1540.

Sunada, S., Takashima, H., Hattori, T., Yasuda, K. & Kawachi, K. (2002). Fluid-dynamic characteristics of a bristled wing, *J. Exp. Biol.* **205**: 2737–2744.

Terry, I. (2001). Thrips and weevils as dual, specialist pollinators of the Australian cycad *macrozamia communis* (Zamiaceae), *Int. J. Plant Sci.* **162**: 1293–1305.

Ullman, D. E., Meideros, R., Campbell, L. R., Whitfield, A. E., Sherwood, J. L. & German, T. L. (2002). Thrips as vectors of tospoviruses, *Adv. Bot. Res* **36**: 113–140.

Weihs, D. & Barta, E. (2008). Comb wings for flapping flight at extremely low Reynolds numbers, *AIAA J.* **46**: 285–288.

Weis-Fogh, T. (1973). Quick estimates of flight fitness in hovering animals, including novel mechanisms for lift production, *J. Exp. Biol.* **59**: 169–230.

Weis-Fogh, T. (1975). Unusual mechanisms for the generation of lift in flying animals, *Sci. Am.* **233**: 81–87.

Whitfield, A. E., Ullman, D. E. & German, T. L. (2005). Tospovirus-thrips interactions, *Annu. Rev. Phytopathol.* **43**: 459–489.

Wu, J. C. (1981). Theory for aerodynamic force and moment in viscous flows, *AIAA J.* **19**: 432–441.

SUPPLEMENTARY MATERIAL

Pausing after clap reduces power required to fling wings apart at low Reynolds number

Vishwa T. Kasoju and Arvind Santhanakrishnan

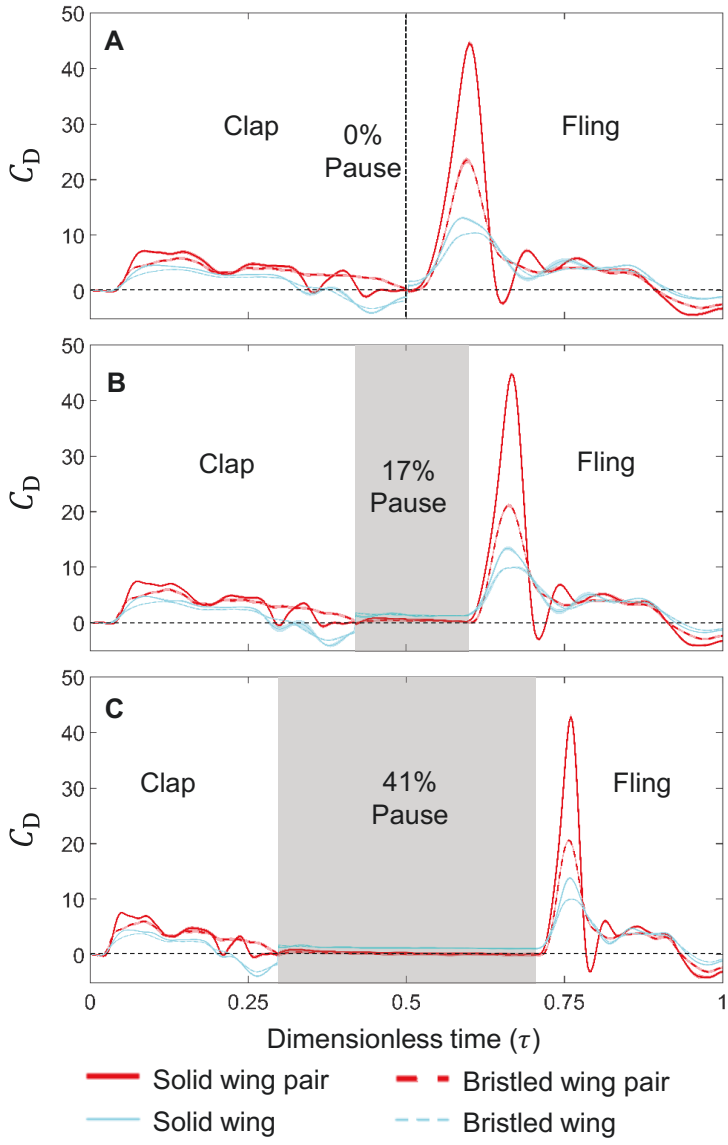

Figure S1. Drag coefficients (C_D) for a single wing and a wing pair at Re_c=10 during an entire cycle (including the pause time). Shading around each curve represents range of ±1 standard deviation for that particular data (across 30 cycles). (A) 0% pause, (B) 17% pause, (C) 41% pause. Grey shaded regions in the figure represents the pause period. Legend is shown at the bottom of the figure.

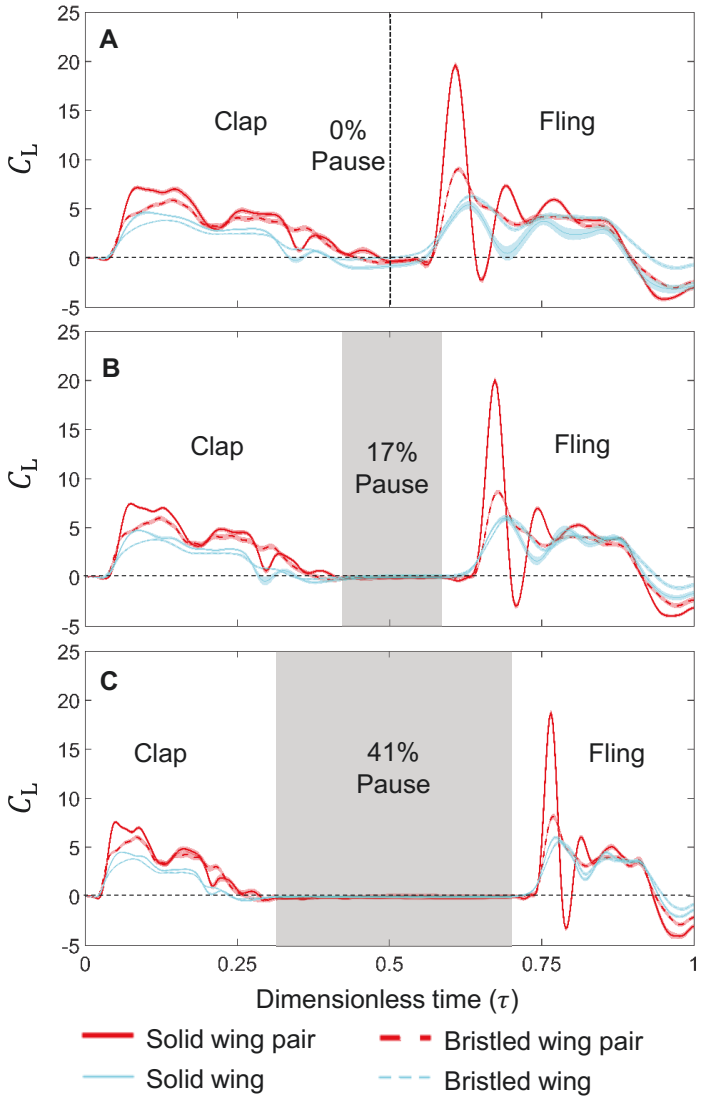

Figure S2. Lift coefficients (C_L) for a single wing and a wing pair at Re_c=10 during an entire cycle (including the pause time). Shading around each curve represents range of ±1 standard deviation for that particular data (across 30 cycles). (A) 0% pause, (B) 17% pause, (C) 41% pause. Grey shaded regions in the figure represents the pause period. Legend is shown at the bottom of the figure.

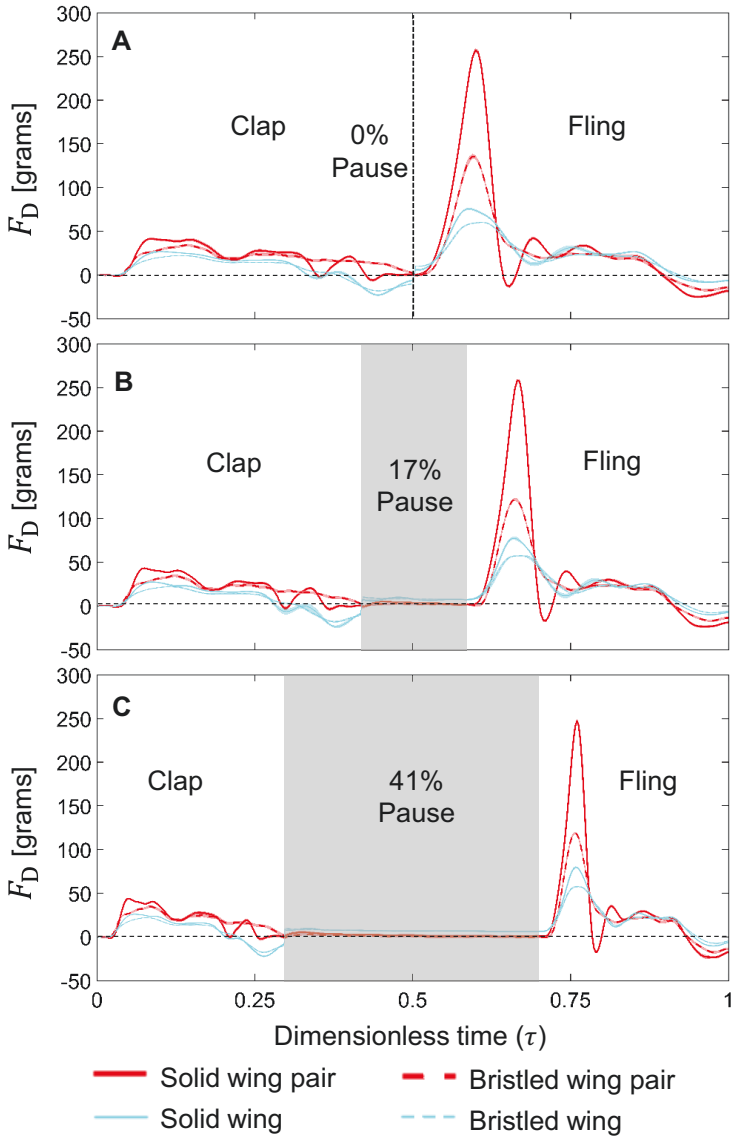

Figure S3. Drag force (F_D) in grams for a single wing and a wing pair at Re_c=10 during an entire cycle (including the pause time). Shading around each curve represents range of ±1 standard deviation for that particular data (across 30 cycles). (A) 0% pause, (B) 17% pause, (C) 41% pause. Grey shaded regions in the figure represents the pause period. Legend is shown at the bottom of the figure.

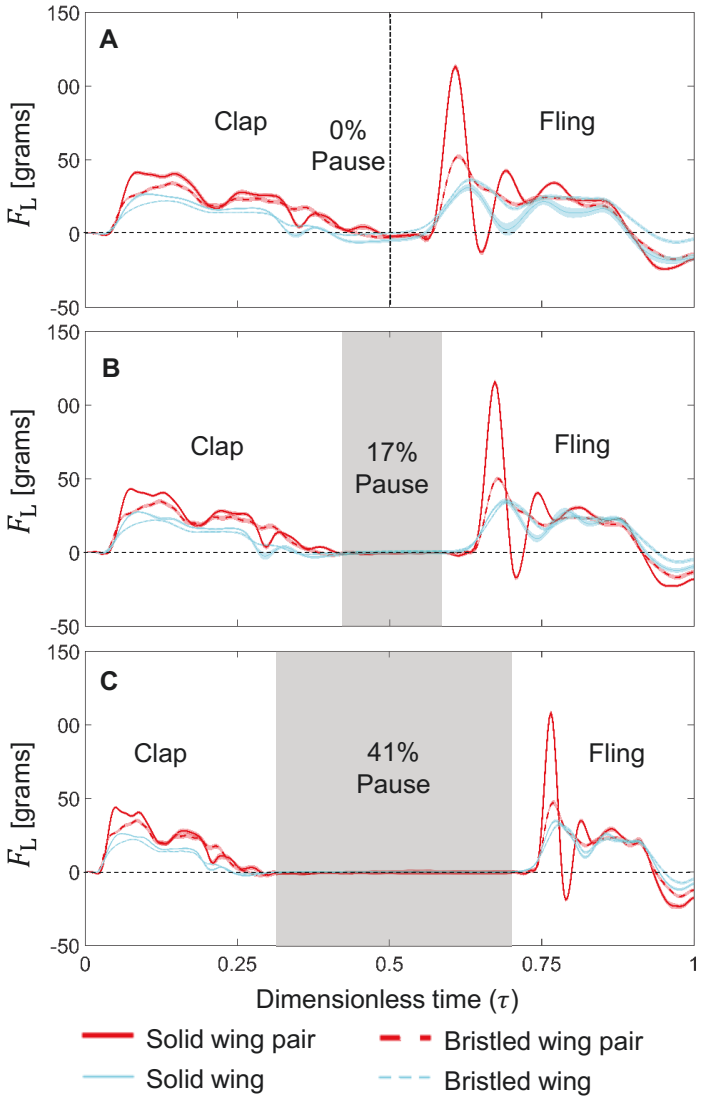

Figure S4. Lift force (F_L) in grams for a single wing and a wing pair at Re_c=10 during an entire cycle (including the pause time). Shading around each curve represents range of ± 1 standard deviation for that particular data (across 30 cycles). (A) 0% pause, (B) 17% pause, (C) 41% pause. Grey shaded regions in the figure represents the pause period. Legend is shown at the bottom of the figure.

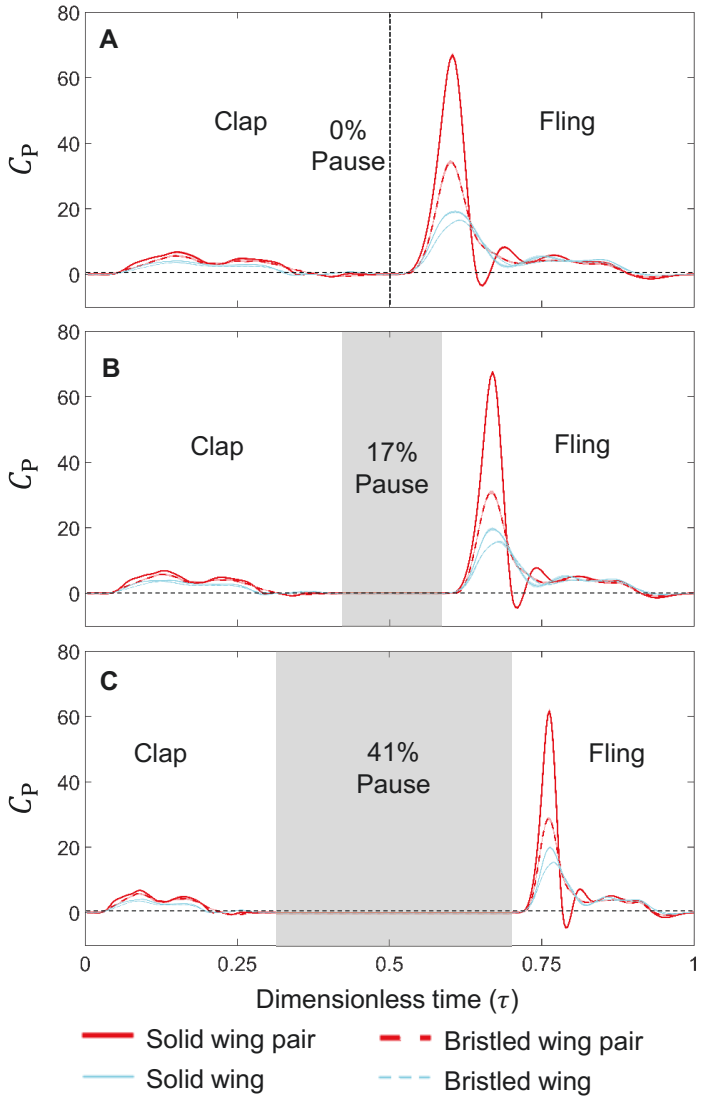

Figure S5. Power coefficients (C_P) for a single wing and a wing pair at Re_c=10 during an entire cycle (including the pause time). Shading around each curve represents range of ±1 standard deviation for that particular data (across 30 cycles). (A) 0% pause, (B) 17% pause, (C) 41% pause. Grey shaded regions in the figure represents the pause period. Legend is shown at the bottom of the figure.

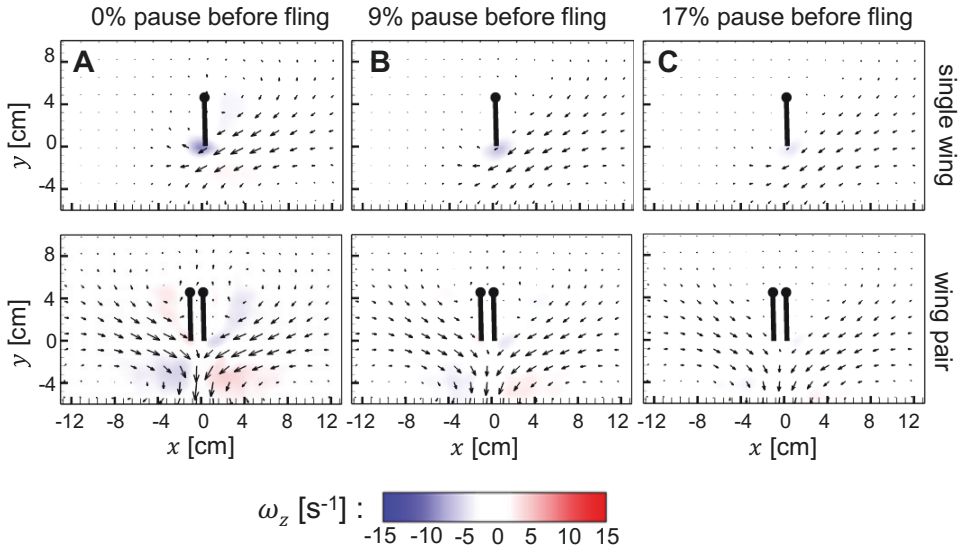

Figure S6. Velocity vector fields overlaid on out-of-plane z-vorticity (ω_z) contours for single solid wing and solid wing pair at $Re_c = 10$ for various pause times just before start of fling (0% of fling time): (A) 0%, (B) 9%, (C) 17% were displayed along each column. Red colour represents counterclockwise vorticity, while blue represents clockwise vorticity. z-vorticity (ω_z) was calculated using equations.